Rea, D.K., Basov, I.A., Janecek, T.R., Palmer-Julson, A., et al., 1993
Proceedings of the Ocean Drilling Program, Initial Reports, Vol. 145

7. SITES 885/886[1]

Shipboard Scientific Party[2]

HOLE 885A

Date occupied: 3 September 1992

Date departed: 4 September 1992

Time on hole: 1 day, 2 hr, 30 min

Position: 44°41.296′N, 168°16.319′E

Bottom felt (rig floor; m, drill-pipe measurement): 5719.9

Distance between rig floor and sea level (m): 11.4

Water depth (drill-pipe measurement from sea level, m): 5708.5

Total depth (rig floor; m): 5778.7

Penetration (m): 58.8

Number of cores (including cores with no recovery): 8

Total length of cored section (m): 58.8

Total core recovered (m): 53.7

Core recovery (%): 91.4

Oldest sediment cored:
Depth (mbsf): 52.3
Nature: clay
Age: late Miocene
Measured velocity (km/s): 1.49

Hard rock:
Depth (mbsf): 58.8
Nature: basalt

Basement:
Depth (mbsf): 58.8
Nature: basalt

HOLE 886A

Date occupied: 4 September 1992

Date departed: 4 September 1992

Time on hole: 5 hr, 15 min

Position: 44°41.384′N, 168°14.416′W

Bottom felt (rig floor; m, drill-pipe measurement): 5724.8

Distance between rig floor and sea level (m): 11.4

Water depth (drill-pipe measurement from sea level, m): 5713.4

Total depth (rig floor; m): 5734.5

Penetration (m): 9.7

Number of cores (including cores with no recovery): 1

Total length of cored section (m): 9.7

Total core recovered (m): 9.7

Core recovery (%): 100

Oldest sediment cored:
Depth (mbsf): 9.7
Nature: clay
Age: Pleistocene
Measured velocity (km/s): 1.5

HOLE 886B

Date occupied: 4 September 1992

Date departed: 5 September 1992

Time on hole: 12 hr, 30 min

Position: 44°41.384′N, 168°14.416′W

Bottom felt (rig floor; m, drill-pipe measurement): 5725.7

Distance between rig floor and sea level (m): 11.4

Water depth (drill-pipe measurement from sea level, m): 5714.3

Total depth (rig floor; m): 5794.6

Penetration (m): 68.9

Number of cores (including cores with no recovery): 9

Total length of cored section (m): 68.9

Total core recovered (m): 60.5

Core recovery (%): 87.8

Oldest sediment cored:
Depth (mbsf): 68.5
Nature: clay
Age: late Miocene
Measured velocity (km/s): 1.5

Hard rock:
Depth (mbsf): 68.9
Nature: basalt

Basement:
Depth (mbsf): 68.9
Nature: basalt

HOLE 886C

Date occupied: 5 September 1992

Date departed: 6 September 1992

Time on hole: 18 hr, 15 min

Position: 44°41.384′N, 168°14.400′W

Bottom felt (rig floor; m, drill-pipe measurement): 5724.7

Distance between rig floor and sea level (m): 11.4

Water depth (drill-pipe measurement from sea level, m): 5713.3

Total depth (rig floor; m): 5797.1

Penetration (m): 72.4

Number of cores (including cores with no recovery): 8

Total length of cored section (m): 72.4

Total core recovered (m): 67.1

[1] Rea, D.K., Basov, I.A., Janecek, T.R., Palmer-Julson, A., et al., *Proc. ODP, Init. Repts.*, 145: College Station, TX (Ocean Drilling Program).
[2] Shipboard Scientific Party is as given in list of participants preceding the contents.

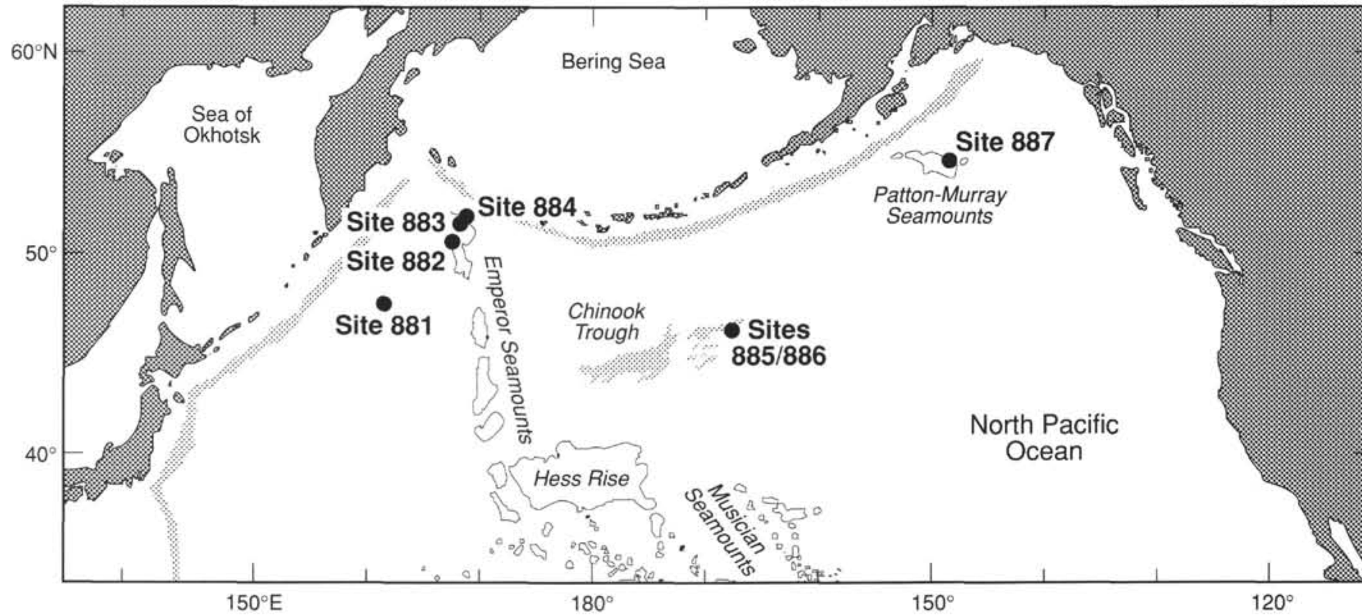

Figure 1. Index map of the North Pacific Ocean showing Leg 145 drill sites.

Core recovery (%): 92.7

Oldest sediment cored:

Depth (mbsf): 72.4

Nature: clay

Age: late Miocene

Measured velocity (km/s): 1.48

Principal results: The site survey for Leg 145 proposed Site NW-4A (Sites 885/886, Fig. 1) began at 0200 hr (local time) on 3 September 1992, only 36 hr after the Golden Dragon had judged all Worms fit for passage across the International Date Line. A beacon was dropped at 0337 hr; the survey was finished and the ship positioned on Site 885 by 0730 hr. The first attempt at an APC core came up water only. The drillers attempted to "feel" bottom with the drill string and were uncertain, so decided to shift the ship's position 400 m east before trying again. At the new offset location, Hole 885A was spudded at 0000 hr on 4 September. Core 145-885A-6H crossed into pelagic clays from the siliceous ooze above, but the barrel on Core 145-885A-7H did not stroke out, and the core returned with basalt chips in the core-catcher sample. A single XCB core (145-885A-8X), was recovered after drilling 6 m and encountering unstable hole conditions. A rubble of basalt and yellow-brown, baked, bricklike rock was recovered from the core-catcher sample. Assuming we had encountered a sill, we offset the ship 2.2 km east to a sediment pond encountered during the site survey, dropped a new beacon, and began Site 886 at 1800 hr on 4 September. Core 145-886A-1H missed the mud line and was full, so we pulled up 7 m and tried again; Core 145-886B-1H recovered the mud line and 1.8 m of siliceous clay. Eight cores were recovered at Hole 886B, reaching basalt at a depth of 68.5 mbsf. The final core (145-886B-9X) came up with only a few rock chips, so we pulled up the drill pipe, offset and spudded Hole 886C at 0630 hr on 5 September. Our intent was to collect a set of cores to overlap with those from Hole 886B. The last core (145-886C-8H) was on deck by 1445 hr, and the *JOIDES Resolution* was under way at 0030 hr on 6 September to the last site of Leg 145, at the Patton-Murray Seamounts in the Gulf of Alaska.

Drilling at Sites 885 and 886 encountered 66 m of sediment overlying basalt. The sediment can be divided into three units: clay with diatoms, diatom ooze, and clay. Unit I (0–17.3 mbsf) is an upper Pliocene to Pleistocene clay containing diatoms and spicules. Unit II (17.3–50.3 mbsf) is an upper Miocene to upper Pliocene diatom ooze with clay. Several large manganese nodules, both brown and black in color, occur at mid-depth in this unit, roughly 40 mbsf. Unit III (50.3–71.9 mbsf in Hole 886C) is clay. This unit is the deep chocolate color of the classic North Pacific Ocean "red" clays. Lithologic Unit IV, 52.1–58.8 in Hole 886A and 68.5–68.9 in Hole 886B, is basalt that has been baked to a yellow brown color and was recovered only as pieces of rubble.

No nannofossils and few foraminifers occur in the section. Diatoms and radiolarians are abundant above 50 mbsf, where they indicate an age of up to 9 Ma. Ichthyoliths were recovered from the underlying pelagic clays. Considering the slow sedimentation rates, we derived a good magnetic reversal stratigraphy for Sites 885/886. A stratigraphy reliable down to anomaly 3 may be possible for both sites. The Matuyama/Gauss reversal boundary occurs at the Unit I/Unit II lithologic boundary in a manner similar to that at all other Leg 145 drill sites. Sedimentation rates are in the range of 5 to 6 m/m.y. in Units I and II and much lower in Unit III. Mineral fluxes in the upper unit are 250 to 300 $mg(cm^2 \cdot k.y.)^{-1}$, exactly the glacial-aged eolian mineral flux recorded elsewhere in the North Pacific Ocean. Silica fluxes are about half that value in the upper unit, but increase two- or three-fold in the lower Pliocene and upper Miocene oozes. Thus, although the rates are much less at Sites 885/886, the latest Miocene through early Pliocene period of extreme silica sedimentation that characterizes sites to the north and west is well displayed here. The unexpected presence of basalt at 66 mbsf means that the deeper/older objectives of this site were not fulfilled, but it points to either a region of seafloor completely devoid of the thin carbonates that underlie the whole North Pacific Ocean, or a sill denoting a volcanic rejuvenation of this region at a time as much as 50 m.y. younger than the age of the seafloor. Either eventuality entails a new understanding of the central North Pacific Ocean.

BACKGROUND AND SCIENTIFIC OBJECTIVES

Site 885 (proposed Site NW-4) is the deepest and most southerly of all the Leg 145 sites. It is situated in the middle of the subarctic Pacific just south of the eastern extremity of the Chinook Trough and far from the Emperor Seamounts and Aleutian Ridge. Continuous seismic profiling records conducted in the region show an approximately 150-m-thick sedimentary sequence of two horizons that presumably consist of Cretaceous-Cenozoic pelagic clay, with some amount of biogenic siliceous component in the uppermost part (transparent unit) overlying Lower(?) Cretaceous limestones with cherts (lower layered unit having strong reflectors). The crustal block that was drilled at Site 885 may once have been part of the minor Chinook Plate, which separated from the Farallon Plate and attached to the

Pacific Plate during the Late Cretaceous tectonic reorganization approximately 82 m.y. ago (Rea and Dixon, 1983).

Several objectives were targeted by drilling at this site. Its location near the subarctic front promised the possibility of determining the timing of the onset of siliceous sedimentation in the North Pacific Ocean and its evolution during the Neogene. Information obtained here and combined with data from other Leg 145 sites, as well as from DSDP Leg 86 sites (Heath, Burckle, et al., 1985) should help to monitor latitudinal excursions of the polar front in response to climatic fluctuations. A continuous late Cenozoic sequence of siliceous clays was expected to provide magnetic reversal stratigraphy and biostratigraphic control, based on diatom and radiolarian zonations.

One of the main goals of Leg 145 drilling that we failed to reach at Site 881 in the Northwest Pacific Basin was expected to be achieved here. The Cretaceous–Cenozoic pelagic clays that have accumulated at abyssal depths far away from sources of ice-rafted and turbidity-current-transported terrigenous material provide one the opportunity to trace the changes in accumulation rates and mineralogy of eolian dust in the North Pacific Ocean. Studies of distributional patterns of wind-transported material in pelagic sections in the central part of the Pacific Ocean (Leinen and Heath, 1981; Janecek and Rea, 1983; Janecek, 1985; Rea et al., 1985) demonstrated dramatic changes in eolian dust supply at the Paleocene/Eocene boundary, at the Oligocene/Miocene boundary, and in the late Pliocene. Data about the flux of eolian material at Site 885 will supplement these previous studies and allow us to estimate the intensity of atmospheric circulation and related climatic fluctuations, as well as the temporal and latitudinal variability of these parameters during the Cretaceous–Cenozoic.

Another aim of drilling at this site was to obtain information concerning the paleoceanographic history of the Cretaceous Pacific Ocean. Before Leg 145 and only in Site 192 (drilled during DSDP Leg 19 on Meiji Seamount) were Cretaceous (Maastrichtian) sediments recovered within the entire subarctic Pacific Ocean (Creager, Scholl, et al., 1973). Drilling at Site 885 was expected to give us a chance (1) to recover a calcareous Lower Cretaceous sequence that had formed (based upon site backtracking) under the productive equatorial zone and (2) to further our understanding of Cretaceous paleoceanography and tectonic evolution of the North Pacific Ocean. Calcareous and siliceous microfossils expected in these sediments should provide constraints for the age of basement formation.

The possible presence of hydrothermally derived components in the sediments of Site 885 should provide a record of hydrothermal activity related to the Chinook Trough rifting episode, as well as additional information for checking ocean chemical anomalies that may have occurred in conjunction with the Cretaceous/Tertiary and Paleocene/Eocene boundaries (Kyte and Wasson, 1986; Owen and Rea, 1985).

To achieve these objectives, two holes were planned at Site 885 with double APC-coring to refusal and a single XCB-cored hole to basaltic basement. No logging was planned for this site.

OPERATIONS

Transit to Proposed Site NW-4A

The 1024-nmi transit to proposed Site NW-4A was marked by the crossing of the International Date Line at 0620 hr (local), 2 September 1992. The Golden Dragon, Guardian of the Mysteries of Time and Defender of the Date Line, was welcomed on board the *JOIDES Resolution* by Captain Oonk at 1300 hr. During the ensuing ceremony, all Worms (creatures who never before had crossed the Date Line) presented a token song or story to His Imperial Goldness and requested rites of passage in return. His Goldness was lenient, and no Worms were cast into the nether regions. At 1500 hr, His Goldness, replete with entourage, departed the ship to check out the action on a tramp steamer bound for the Far East.

At 0145 hr, 3 September, the ship slowed to 6 kt to deploy the seismic equipment and begin a 22-nmi survey. At 0330 hr, a beacon was launched on site as the ship continued with the survey. At 0630 hr, the seismic equipment was pulled in, and the ship acquired a beacon signal at 0730 hr. By 0800 hr, the ship was on location, with hydrophones and thrusters lowered.

Hole 885A

The first mud-line core was attempted at 1715 hr, 3 September, but was shot too high in the water column. The pipe was lowered until the formation appeared to take 20,000 lb of weight on bit at a depth of 5714 m below the rig floor (mbrf). The pipe was lifted up to 5711 mbrf, and a second attempt to obtain a mud-line core resulted in yet another water core. We then attempted to re-tag bottom at 5714 mbrf, with no success. We assumed that the bottom was hilly and potentially dangerous for operating the drill string. The vessel was offset 400 m east to what appeared to be much flatter terrain, and the drill pipe was lowered to what was thought to be 5715.0 mbrf. A third spud-in attempt at 2230 hr also resulted in a water core. This third spud-in failure was the result of a miscounting of the number of stands of pipe connected to the drill string.

At 2330 hr, Hole 885A finally was spudded, and 4.6 m of sediment was recovered in Core 145-885A-1H, resulting in a mud-line depth of 5719.9 mbrf (see Table 1 for a summary of coring operations). Piston-coring advanced the drill string to 52.3 mbsf (Core 145-885A-7H), where a hard contact (basement) prevented a full stroke. The last core of this hole was an XCB attempt (Core 145-885A-8X) that advanced 6.5 m and from which was recovered 0.42 m of basalt and baked clay fragments. APC-coring penetrated 52.3 m and recovered 53.22 m (91.2% recovery). Total recovery was 53.64 m over a cored interval of 58.8 m (91.2% recovery). Cores 145-885A-4H through -7H were oriented. After Core 145-885A-8X was retrieved, the pipe was pulled out of the hole; the bit cleared the mud line at 1000 hr, 4 September.

Hole 886A

The ship was offset to what appeared to be a thicker sediment pond, located about 2200 m east of Site 885. At 1230 hr, 4 September, a new beacon was deployed and, consequently, the next hole was designated Hole 886A.

At 1500 hr, the first mud-line core was attempted at a depth of 5666 mbrf, but this resulted in yet another water core. After a second mud-line core was attempted at 5680 mbrf and also resulted in a water core, the position depth recorder settings were examined. The pulse-width setting on the transmitter was found to have been set at 25 ms instead of 100 ms, resulting in a depth error reading of about 57 m. The next mud-line core was attempted at a depth of 5725 mbrf. The resulting core barrel was full and unsuitable for assigning a mud-line depth. However, this core was used for high-resolution, interstitial-water and physical property analyses.

Hole 886B

Hole 886B was spudded with a successful mud-line core at 1900 hr, 4 September. The resulting depth of the mud line was determined as 5725.7 mbrf. Piston-coring advanced to 58.8 mbsf (Core 145-886B-7H), where 59.28 m was recovered (100.8% recovery). To avoid a hard impact with the basement, coring was switched over to the XCB-coring system; Core 145-886B-8X advanced 9.7 m, but only 0.81 m was recovered. The next core was able to advance only 0.4 m in 30 min of rotation, with 0.41 m of basalt fragments recovered. The pipe was pulled out of the hole after Core 145-886B-9X, and the vessel was offset 20 m east.

Hole 886C

Hole 886C was spudded at 0645 hr, 5 September; Core 145-886C-1H contained 6.86 m of sediment upon recovery and established the mud line at 5724.7 mbrf. Piston-coring advanced 72.4 m (Core 145-886C-8H), and 67.09 m was recovered (92.7% recovery). After Core 145-886C-9H was brought on deck, the pipe was pulled out of the hole. While the pipe was being pulled out of the hole, the two beacons at this site were recalled and collected in heavy fog. The vessel then was offset to Site 885, and the remaining beacon was recalled and extracted from the fog and dark, thanks to the effectiveness of the flasher on the beacon. By 0030 hr, 6 September, the ship was under way to the last site.

LITHOSTRATIGRAPHY

Introduction

Sites 885/886 (Fig. 1) are located 2.3 km apart; the sediments recovered at each exhibit similar lithostratigraphic sequences. For these reasons, the sediments from both sites are discussed here as a combined sediment column.

The gross sediment composition at Sites 885/886 reflects a variable mixture of two major lithologic end-members: clay and diatom ooze. Three major lithologic units can be recognized; these are based upon the relative abundance, of these two lithologies; as determined by smear slide analyses (Fig. 2). Unit I is composed predominantly of clay, with diatoms and spicules as minor lithologies; Unit II, of diatom ooze and clayey diatom ooze; and Unit III, of clay and hematitic clay. These three units overlie a fourth major lithologic unit that consists of altered basalt cobbles. The sedimentary sequence is approximately 72 m thick and ranges in age from Pleistocene to late Miocene for the interval from 0 to 54.3 mbsf. Sediments below 54.3 mbsf are either barren or contain nondiagnostic fossil assemblages (see "Biostratigraphy" section, this chapter).

Description of Units

The depth intervals reported below for each lithologic unit are based upon significant changes in diatom and clay abundances in the combined smear slide analyses for all cores collected at Sites 885 and 886 (Fig. 3). The depth intervals for each lithologic unit at each hole drilled at Sites 885/886 are summarized in Table 2. Four samples from sediments recovered at Sites 885/886 were analyzed for trace-element geochemistry by XRF; those data are presented in Table 3.

Unit I

Intervals: Cores 145-885A-1H to -2H
Core 145-886-A-1H
Cores 145-886B-1H to -4H
Cores 145-886C-1H to -3H
Depth: 0–17.3 mbsf
Age: Pleistocene to late Pliocene

Unit I is characterized by reddish-brown and brown clay in concentrations that typically range from 65% to 95%. Diatoms (4%–15%) and spicules (1%–30%) are present as minor lithologies, with spicule concentrations increasing from 1% to 15% in the upper (0–9 mbsf) part of the unit to 25% to 30% in the lower part.

Subordinate lithology includes pyrite and volcanic ash layers. Pyrite occurs in the upper 9 m of the unit in various forms, including distinct altered concretions about 2 cm in diameter that exhibit limonitic surface staining, as concretions of agglomerated crystals, and as an intergranular cement in ash-filled burrows. Two distinct ash layers that are 1 and 3 cm thick, respectively, are seen in Hole 885A, Core 145-885A-2H. Both ash layers exhibit gradational upper and sharp lower contacts. Similar ash layers are not present in the Site 886 cores, but any ash layers originally present may have been obscured by bioturbation. The effects of bioturbation are evident throughout the unit, as indicated by the occurrence of black ash-filled burrows and mottles and pockets of white to gray spicule oozes.

Table 1. Summary of coring operations, Sites 885/886.

Core no.	Date (Sept 1992)	Time (UTC)	Depth (mbsf)	Length cored (m)	Length recovered (m)	Recovery (%)
Hole 885A						
1H	4	1055	0.0–4.6	4.6	4.57	99.3
2H	4	1200	4.6–14.1	9.5	9.48	99.8
3H	4	1300	14.1–23.6	9.5	9.83	103.0
4H	4	1400	23.6–33.1	9.5	9.97	105.0
5H	4	1510	33.1–42.6	9.5	9.77	103.0
6H	4	1630	42.6–52.1	9.5	9.51	100.0
7H	4	1745	52.1–52.3	0.2	0.17	85.0
8X	4	2045	52.3–58.8	6.5	0.42	6.5
Coring totals				58.8	53.72	91.4
Hole 886A						
1H	5	0520	0.0–9.7	9.7	9.70	100.0
Coring totals				9.7	9.70	100.0
Hole 886B						
1H	5	0625	0.0–1.8	1.8	1.76	97.8
2H	5	0730	1.8–11.3	9.5	9.76	103.0
3H	5	0830	11.3–20.8	9.5	9.18	96.6
4H	5	0950	20.8–30.3	9.5	8.76	92.2
5H	5	1105	30.3–39.8	9.5	9.99	105.0
6H	5	1205	39.8–49.3	9.5	9.84	103.0
7H	5	1325	49.3–58.8	9.5	9.99	105.0
8X	5	1450	58.8–68.5	9.7	0.81	8.4
9X	5	1625	68.5–68.9	0.4	0.41	100.0
Coring totals				68.9	60.50	87.8
Hole 886C						
1H	5	1815	0.0–6.8	6.8	6.86	101.0
2H	5	1930	6.8–16.3	9.5	8.47	89.1
3H	5	2025	16.3–25.8	9.5	9.54	100.0
4H	5	2125	25.8–35.3	9.5	9.35	98.4
5H	5	2225	35.3–44.8	9.5	4.55	47.9
6H	5	2330	44.8–54.3	9.5	9.95	105.0
7H	6	0030	54.3–63.8	9.5	9.77	103.0
8H	6	0145	63.8–72.4	8.6	8.60	100.0
Coring totals				72.4	67.09	92.7

Unit II

Intervals: Cores 145-885A-3H to -6H
Cores 145-886B-4H to -7H
Cores 145-886C-3H to -6H
Depth: 17.3–50.3 mbsf
Age: late Pliocene to late Miocene

This unit is composed of light brown to yellowish-brown diatom ooze. Diatom abundances range from 54% to 95% and average 81%. Dark brown clayey diatom ooze occurs as a minor lithology in the lowermost 3 to 5 m of Unit II at Holes 886B and 886C and marks the transition from Unit II to the clays of Unit III. Limonite and ferro-manganese nodules, nodule fragments, and concretions are scattered throughout this unit, particularly in the lower half. The limonite is present as burrow fill and as a coating around pumice fragments. The ferro-manganese nodules are brown and black, 6 to 8 cm in diameter, botryoidal in shape, and typically exhibit well-developed concentric internal structures with multiple volcaniclastic cores (Fig. 3). Only one distinct ash layer, which occurs in Hole 886C at 33.8 mbsf (interval 145-886C-4H-6, 49-51 cm), is present. Slight bioturbation throughout the unit is indicated by black ash filled burrows and scattered white pockets and mottles of spicule ooze.

Unit III

Intervals: Cores 145-885A-6H to -6H
Cores 145-886B-7H to -8X
Cores 145-886C-7H to -8H
Depth: 50.3–71.9 mbsf
Age: late Miocene

Unit III consist of predominantly light to dark brown clay and grades to dark brown hematitic clay at the base of the unit. This unit

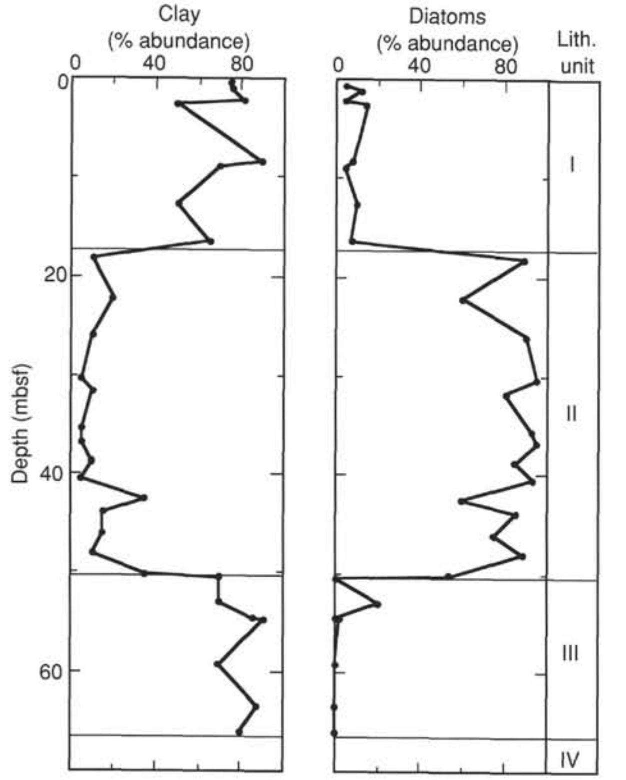

Figure 2. Definition of lithologic units (based on clay and diatom abundances) for the composite sediment column. Data shown are the results of smear slide analyses for all cores recovered at Sites 885 and 886.

is the classic North Pacific "red" clay. In contrast to Unit I, the clays of Unit III typically contain 10% to 30% accessory minerals of authigenic and/or diagenetic origin (Fig. 4). These accessory lithologies include zeolite, hematite, chert and ferro-manganese oxide concretions, and ferro-manganese nodules. The chert and ferro-manganese oxide concretions are <1 cm in diameter and occur in layers 3 to 5 cm thick. The ferro-manganese nodules are similar to those observed in Unit II (i.e., they are black, 3 to 7 cm in diameter, botryoidal or spherical in shape, and exhibit well-developed concentric internal structures with multiple volcaniclastic cores).

Unit IV (Basalt)

Unit IV consists of highly altered palagonitic basaltic cobbles with remnants of a glassy rim and surrounded by a weathered surface (see "Igneous Petrology" section, this chapter).

Discussion

Sediments deposited at Sites 885/886 since late Miocene time record variations in the supply of biogenic silica and terrigenous clastics and the formation of authigenic minerals.

The well-defined interval of increased abundances of diatom vs. clay (Fig. 2) that identifies Unit II at Sites 885/886 potentially could expand both the temporal and spatial record of the late Miocene to late Pliocene interval of enhanced biogenic silica supply in the North Pacific Ocean. This event has not been observed in correlative sediments at similar latitudes, except farther to the west (e.g., DSDP Leg 86, Heath, Burckle, et al., 1985), and apparently occurs about 1 m.y. earlier at Sites 885/886 than at Sites 881 through 884 or other North Pacific Ocean locations (e.g., Barron and Baldauf, 1990). However, interpretation of the paleoceanographic significance of this record is constrained by the absence of robust age control for the sediments in Unit III, which in turn affects sedimentation rate and MAR calculations. If one assumes that the sedimentation rates before and after the event of enhanced site supply are similar, as they are at the Leg 145 sites to the west, then preliminary calculations (see "Sedimentation Rates and Fluxes" section, this chapter) suggest that the silica flux in Unit II is an order of magnitude greater than that in Units I and III, but is lower by a factor of 5 to 10 than that observed at Site 884 to the northwest.

The occurrence of centimeter-scale ferro-manganese nodules and authigenic mineral assemblages, including zeolites and iron oxides in Units II and III, is consistent with both the low sedimentation rates and low amounts of organic carbon determined for these sediments

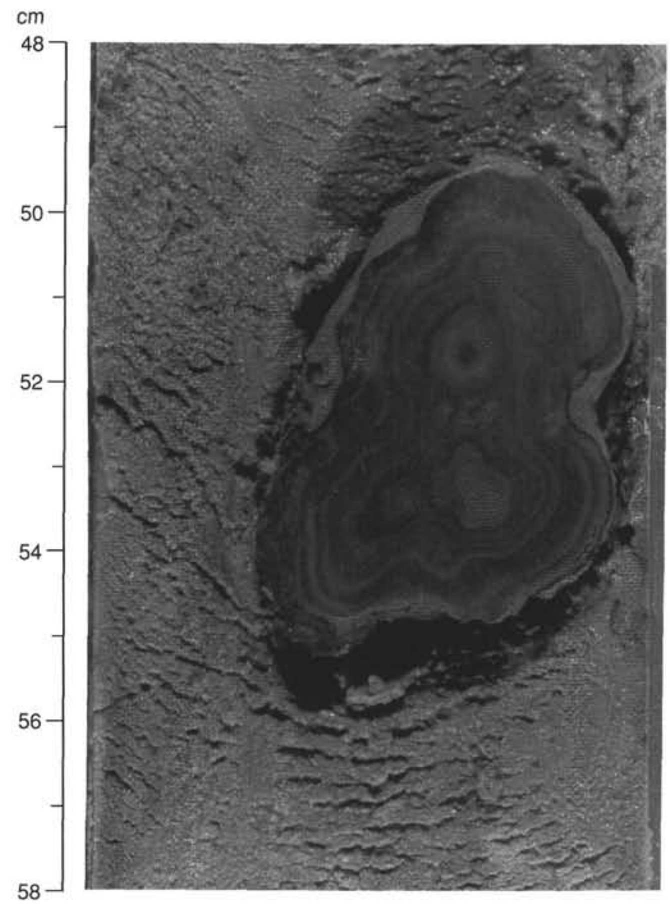

Figure 3. Example of a ferromanganese nodule recovered in Unit II. Nodule shown is black, about 6 cm in diameter, botryoidal in shape, and exhibits well-developed concentric internal structures with multiple volcaniclastic cores.

Table 2. Depth intervals for each lithologic unit at each hole drilled at Sites 885/886.

Lithologic unit	Intervals (cm)	Depth (mbsf)
I	885A-1H to -2H-CC, 20	0–14.1
	886A-1H	0–9.4
	886B-1H to -4H-4	0–25.3
	886C-1H to -3H, 80	0–17.1
II	885A-3H to -6H-3, 20	14.1–45.8
	886B-4H-4 to -7H-3	25.3–52.3
	886C-3H-1, 80 to -6H	17.1–54.3
III	885A-6H, 20 to -6H-CC, 10	45.8–52.1
	886B-7H-3 to -8X-CC	52.3–68.5
	886C-7H to -8H-CC, 5	54.3–72.4
IV	886C-8H-CC, 5–10	72.4–72.45

Table 3. Results of trace-element analysis for samples from Sites 885/886 by shipboard XRF.

Hole	Interval (cm)	Nb	Zr	Y	Sr	Rb	Zn	Cu	Ni	Cr	V	TiO_2	Ba
885A	5H-3, 69–70	6.2	82.7	10.4	97.8	58.2	50.4	102.7	53.2	30.6	46.0	0.28	2983.3
886B	1H-1, 67–69	10.8	164.0	17.9	173.1	104.5	111.4	148.4	87.5	64.1	130.1	0.69	1748.7
886B	4H-1, 67–69	5.9	104.1	11.2	119.0	60.9	81.5	139.6	94.9	26.4	56.8	0.35	3064.8
886B	5H-4, 68–70	5.2	78.2	7.0	91.5	46.7	41.7	86.8	47.0	20.9	49.0	0.27	2532.7

Note: Abundances given in ppm for all elements except TiO_2; TiO_2 concentrations are in weight %.

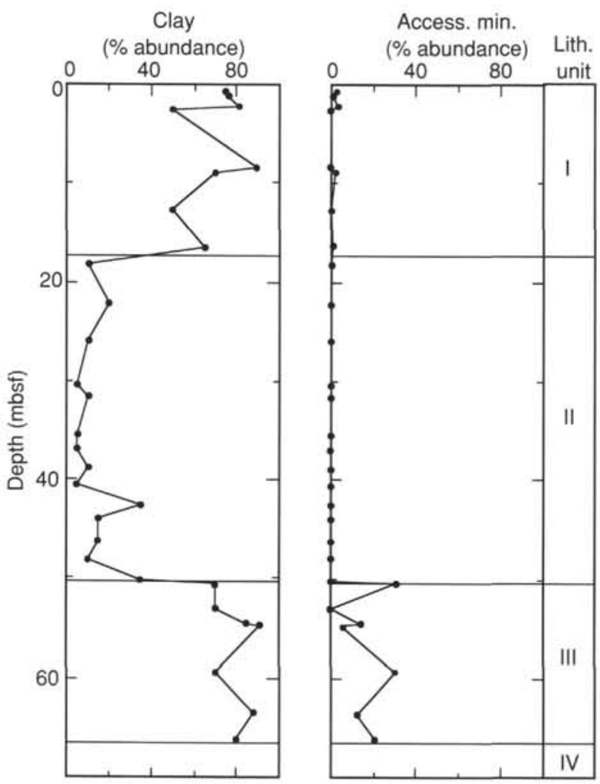

Figure 4. Comparison of clay and accessory mineral abundances in each lithologic unit. Note that the clay-dominated Units I and III primarily differ because of the accessory minerals in Unit III. Accessory minerals include zeolite, hematite, co-mixed chert and ferromanganese oxide concretions, and ferromanganese nodules.

(see "Sedimentation Rates and Fluxes" and "Organic Geochemistry" sections, this chapter). Preservation of large nodules requires a highly oxidizing depositional and diagenetic environment, while both the nodules and the zeolite-iron oxide assemblage are most commonly found in carbonate-free regions of slowly deposited reddish-brown clays and siliceous oozes (Cronan, 1980).

Studies of the relative accumulation rates of several chemical parameters (iron, opal, calcium carbonate, Sr/Ca, and Mn) have suggested the hypothesis that at least certain regions of the Pacific Ocean experienced an episode of significantly intensified hydrothermal activity resulting from late Miocene tectonic reorganizations and volcanism (Owen and Rea, 1985; Lyle et al., 1986). Ferro-manganese nodules formed at that time may have recorded information that would serve to constrain the duration and delimit the geographic scope of such an episode. Bulk nodule compositions reflect the accretion of chemical elements from three distinct end-members: (1) hydrogenous sources (i.e., background seawater), (2) hydrothermal sources (including seawater whose composition has been altered through contributions from hydrothermal effluents), and (3) diagenetic fluids (Chester, 1990). Several factors suggest that diagenetic fluids did not contribute significantly to the compositions of the nodules in Units II and III. These factors include the rounded or botryoidal shape of the nodules, the low amounts of organic carbon in the sediments, the preservation of centimeter-scale nodules at depths tens of meters below the surface, and the presence of other oxidized forms of iron at nodule horizons. Nodules formed under the influence of hydrogenous vs. hydrothermal sources differ in terms of their growth rates, mineralogy, and abundances of major and trace elements (Chester, 1990). Consequently, detailed compositional analyses of the nodules recovered at Sites 885/886 should provide additional insight into the paleochemistry of the Pacific Ocean during the late Miocene.

IGNEOUS PETROLOGY

The two deepest cores from Hole 885A (Cores 145-885A-7H and -8X, 52.1–58.8 mbsf) consist of approximately 60 cm of angular cobbles of moderately altered, aphyric basalt. Some of the cobbles are coated with burnt orange-to-black alteration products. The two cores were placed into two separate lithologic units, because one of the cobbles in the top of Core 145-885A-8X has an altered glassy margin; however, no apparent lithologic differences can be seen between the two units. Extremely rare, moderately altered plagioclase and even rarer olivine microphenocrysts occur in a microcrystalline grounmass. The olivines have been completely altered to iddingsite. No bottom margin was recovered; thus, the structure of the basalt is unknown.

The deepest core from Hole 886B (Core 145-886B-9X, 68.5–68.9 mbsf) consists of approximately 70 cm of angular cobbles of highly altered, aphyric basalt essentially identical to the basalt cobbles recovered from Hole 885A. Cobbles from Hole 886B, however, appear to be more altered, and none has a glassy margin. Many of the cobbles are coated with yellow to burnt orange to black alteration products. Extremely rare, moderately altered plagioclase and even rarer olivine microphenocrysts occur in a microcrystalline groundmass. The olivines have been completely altered to iddingsite. Because no evidence of the nature of the top and bottom margins of the unit was recovered, its structure is unknown.

BIOSTRATIGRAPHY

The upper 58 m of sediments recovered at Sites 885 and 886 contains siliceous fossils that range in age from late Miocene through Quaternary. No calcareous nannofossils are present in any of the core-catcher samples examined at either site. Isolated foraminifers are found in a few samples. Diatoms and radiolarians are abundant in approximately the upper 50 m. Concentrations of siliceous flora and fauna decrease rapidly below this level, with sediments that apparently contain only fish teeth below the interval from 52 to 58 mbsf. The oldest diatom-bearing sediments at Sites 885/886 are approximately 7.5 and 9.0 Ma, respectively.

Foraminifers

All core-catcher samples from Holes 885A and 886B were processed and examined for foraminifers. All samples from Hole 885A are barren. Three samples from Hole 886B (Samples 145-886B-2H-CC, -3H-CC, and -6H-CC) contain rare occurrences of a single species of *Spiroloculina*. No planktonic foraminifers were found.

Radiolarians

Radiolarians present in sediments from core-catcher samples from Sites 885 and 886 range in age from Miocene through Quaternary. In most of the samples examined, radiolarians are common to abundant. Specimens are generally moderately well to well preserved; however, breakage increases markedly below 40 mbsf. Sediments below 59 mbsf do not contain radiolarians. Analysis of only core-catcher material combined with the relatively low sedimentation rate (~5 m/m.y.) and absence of several diagnostic radiolarian species make it difficult to place the various faunal data precisely within any specific zonal scheme.

The radiolarian fauna in Sample 145-886B-1H-CC is representative of the late Quaternary *Botryostrobus aquilonaris* Zone (Hays, 1970), based on the presence of *B. aquilonaris* and *Lychnocanoma grande*, combined with the absence of *Druppatractus acquilonius* and *Stylatractus universus*. Samples 145-885A-1H-CC and -886C-1H-CC contain radiolarian fauna characteristic of the late Quaternary *S. universus* Zone (Hays, 1970), with the presence of both *D. acquilonius* and *S. universus* and the absence of *Eucyrtidium matuyamai*. The early Quaternary *E. matuyamai* Zone (Hays, 1970; Foreman, 1975) is present in sediments from Sample 145-886B-2H-CC, based on the occurrence of *E. matuyamai*.

The presence of *Cycladophora davisiana* var. *davisiana* and *Lamprocyrtis heteroporos* and the absence of *E. matuyamai* and *Stichocorys peregrina* in sediments from Sample 145-886A-1H-CC place this sample most likely within the late Pliocene *L. heteroporos* Zone (Hays, 1970; Foreman, 1975). Succeeding samples from core-catcher samples in Hole 885A (Samples 145-885A-2H-CC and -3H-CC), Hole 886B (Sample 145-886B-3H-CC), and Hole 886C (Sample 145-886C-2H-CC) contain an apparently early Pliocene to early late Pliocene radiolarian fauna, with the presence of *L. heteroporos*, *D. acquilonius*, and *Sphaeropyle langii* and the absence of *C. davisiana* var. *davisiana*, *Theocorys redondoensis*, and *Botryostrobus bramlettei*.

The absence of *S. langii* and the presence of *B. bramlettei* in Samples 145-886B-4H-CC and -886C-3H-CC suggest that sediments from these samples are latest Miocene/earliest Pliocene in age. Samples 145-885A-4H-CC, -886B-5H-CC, and -886C-4H-CC appear to contain a typical late Miocene North Pacific fauna. *S. peregrina* and *Stichocorys delmontensis* are present in these samples in addition to *D. acquilonius* and *B. bramlettei*. The next sequence of samples (Samples 145-885A-5H-CC, -886B-6H-CC) appears to be somewhat earlier late Miocene in age because of the additional presence of both *Stichocorys wolffii* and *Cyrtocapsella cornuta*. Although Sample 145-886C-5H-CC does not contain *S. wolffii*, its radiolarian assemblage is otherwise similar to that in sediments from Samples 145-885A-5H-CC and -886B-6H-CC in Holes 885A and 886B, respectively.

The fauna in Sample 145-885A-6H-CC is similar to that which directly precedes it (Sample 145-885A-5H-CC), except for the absence of both *D. acquilonius* and *S. peregrina*, which may indicate a slightly earlier late Miocene age for these sediments. Sample 145-886C-6H-CC contains *S. delmontensis*, *T. redondoensis*, *C. cornuta*, and *Cyrtocapsella tetrapera*, as well as rare *Lychnocanoma nipponica magnacornuta*. This faunal assemblage limits the age for this sample to between late middle Miocene and early late Miocene.

The few radiolarians present in sediments from Sample 145-886B-7H-CC are not age-diagnostic. Samples from Cores 145-885A-7H and -8X, Cores 145-886C-7H and -8X, and Cores 145-886B-8X and -9X do not contain radiolarians.

Diatoms

Site 885

Diatoms are abundant to common and display good to moderate preservation in the first five cores of Hole 885A (0–42.6 mbsf) and are present down to Section 2 of Core 145-885A-6H (about 45 mbsf). Diatom assemblages are typical of the subarctic North Pacific Ocean, although warm-water taxa, such as *Hemidiscus cuneiformis*, *Nitzschia reinholdii*, and *Thalassiosira convexa*, are typically present, especially in the Pliocene section. The core-catcher samples examined range from the late Pleistocene *Simonseniella curvirostris* Zone (145-885A-1H-CC) to the late Miocene *Thalassionema schraderi* Zone (145-885A-6H-CC) (Fig. 5).

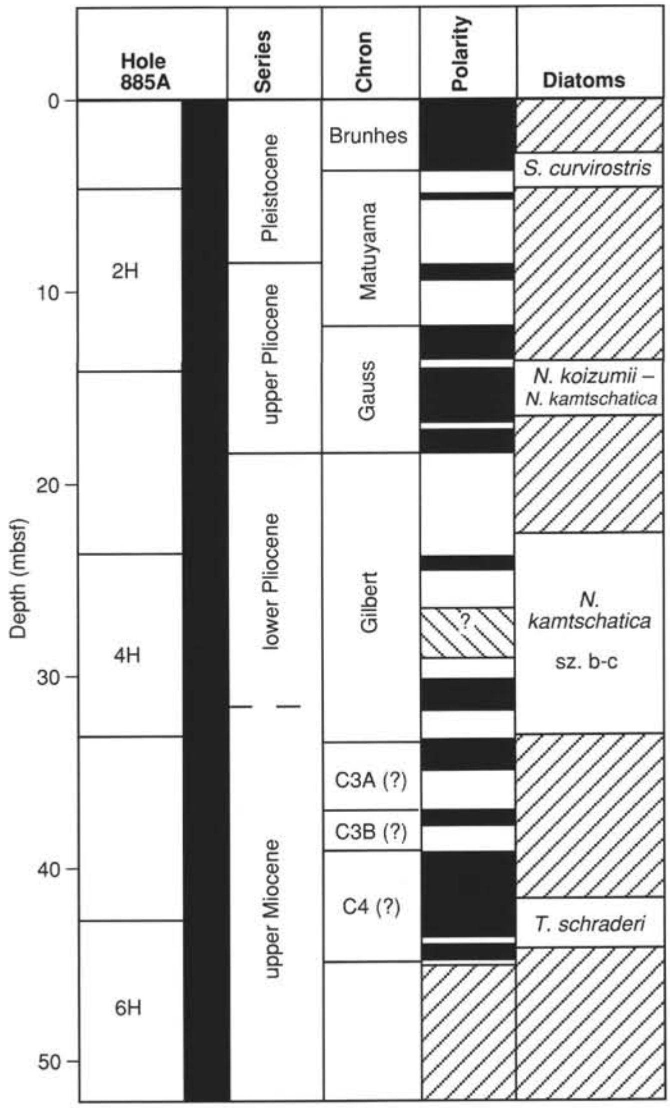

Figure 5. Stratigraphic position of core, recovery (black), ages, placement of magnetostratigraphic chrons and subchrons, polarity log, and placement of diatom zones in Hole 885A. Intervals filled by slanted lines indicate uncertainty in the placement of magnetostratigraphic and biostratigraphic boundaries.

Site 886

At Site 886, abundant-to-common diatoms are present in Cores 145-886A-1H, -886B-1H through -6H, and -886C-1H through -5H, or above about 50 mbsf. Preservation of these diatoms is generally good to moderate in this interval, and the assemblages can be readily zoned using the Leg 145 North Pacific diatom zonation (Table 4). Recognized zones in this interval range from the late Pleistocene *Neodenticula seminae* Zone (Sample 145-886B-1H-CC [4.6 mbsf]) through the late Miocene *Thalassionema schraderi* Zone (Sample 145-886B-6H-CC [49.3 mbsf]). A poorly preserved assemblage in Sample 886C-6H-CC (54.3 mbsf) that contains *Denticulopsis dimorpha* has been tentatively assigned to the early late Miocene *D. dimorpha* Zone (Fig. 6). Within the middle part of the Pliocene (Samples 145-886B-3H-CC [20.8

Table 4. Age and stratigraphic position of radiolarian (R) and diatom (D) datum levels in Holes 885A, 886A, 886B, and 886C.

Sample		Datum	Age (Ma) CK92	Hole 885A		Holes 886A, 886B, and 886C	
				Interval	Depth (mbsf)	Interval	Depth (mbsf)
R1	LO	*Lychnocanoma grande*	0.05	<1H-CC	<4.6	<B1H-CC	<1.8
D2	LO	*Simonseniella curvirostris*	0.3	<1H-CC	<4.6	B1H-CC/C1H-CC	1.8/6.8
R2	LO	*Druppatractus acquilonius*	0.35	<1H-CC	<4.6	B1H-CC/C1H-CC	1.8/6.8
R3	LO	*Stylatractus universus*	0.45	<1H-CC	<4.6	B1H-CC/C1H-CC	1.8/6.8
D5	LCO	*Actinocyclus oculatus*	1.00	1H-CC/2H-CC	4.6/14.1	C1H-CC/A1H-CC	6.8/9.7
R5	LO	*Eucyrtidium matuyamai*	1.05	1H-CC/2H-CC	4.6/14.1	C1H-CC/B2H-CC	6.8/11.3
D6	FO	*Simonseniella curvirostris*	1.58	1H-CC/2H-CC	4.6/14.1	B2H-CC/C2H-CC	11.3/15.27
R7	FO	*Eucyrtidium matuyamai*	1.9	1H-CC/2H-CC	4.6/14.1	B2H-CC/C2H-CC	11.3/15.27
D9	LO	*Neodenticula koizumii*	2.0	1H-CC/2H-CC	4.6/14.1	B2H-CC/C2H-CC	11.3/15.27
D12	LCO	*Neodenticula kamtschatica*	2.63–2.7	1H-CC/2H-CC	4.6/14.1	B2H-CC/C2H-CC	11.3/15.27
R8	FO	*Cycladophora davisiana*	2.8	1H-CC/2H-CC	4.6/14.1	B2H-CC/C2H-CC	11.3/15.27
R9	LO	*Stichocorys peregrina*	2.9	3H-CC/4H-CC	23.6/33.1	B4H-CC/C4H-CC	30.3/35.3
D17	FO	*Neodenticula koizumii*	3.75	2H-CC/3H-CC	14.1/23.6	C2H-CC/B3H-CC	16.3/20.8
D16	FO	*Actinocyclus oculatus*	3.8	2H-CC/3H-CC	14.1/23.6	C3H-CC/B4H-CC	25.8/30.3
R11	LO	*Theocorys redondoensis*		4H-CC/5H-CC	33.1/42.6	B5H-CC/C5H-CC	39.8/44.8
R12	FO	*Lamprocyrtis heteroporos*	4.6	4H-CC/5H-CC	33.1/42.6		
D19	FO	*Thalassiosira latimarginata*	5.05	3H-CC/4H-CC	23.6/33.1	B4H-CC/C4H-CC	30.3/35.3
D21	FO	*Thalassiosira oestrupii*	5.4	4H-CC/5H-CC	33.1/42.6	C5H-CC/B6H-CC	39.85/49.3
R	FO	*Druppatractus acquilonius*	6.75	5H-CC/6H-CC	42.6/52.1	C5H-CC/B6H-CC	49.3/54.3
D25	FO	*Neodenticula kamtschatica*	7.25	4H-CC/5H-CC	33.1/42.6	C5H-CC/B6H-CC	39.85/49.3
D26	LCO	*Thalassionema schraderi*	7.45	4H-CC/5H-CC	33.1/42.6	C5H-CC/B6H-CC	39.85/49.3
R	LO	*Lychnocanoma nipponica magnacornuta*	8.5	Not seen		C5H-CC/C6H-CC	44.8/54.3
D32	LO	*Denticulopsis dimorpha*	9.0	Not seen		B6H-CC/C6H-CC	49.3/54.3
R	FCO	*Stichocorys peregrina*	6.75	5H-CC/6H-CC	42.6/52.1	B6H-CC/C6H-CC	49.3/54.3

Notes: Samples constraining each datum level are separated by a slash (/), as are the sub-bottom depths (mbsf) of these samples. LO = last occurrence ; LCO = last common occurrence ; FO = first occurrence; and FCO = first common occurrence. CK92 refers to the Cande and Kent (1992) geomagnetic polarity time scale.

mbsf] and -886C-3H-CC [25.8 mbsf]), the diatom assemblage contains *Actinocyclus oculatus*, but lacks *Neodenticula koizumii*. The FO of these two taxa is observed to be roughly equivalent at Leg 145 Sites 882, 883, and 884; thus, it is likely either that *N. koizumii* has been ecologically excluded in these relatively warm-water assemblages or that it has been removed by dissolution. The scarcity of *N. kamtschatica* in these samples supports either hypothesis. Thus, one can assume that Samples 145-886B-3H-CC and -886C-3H-CC are equivalent in age to the *N. koizumii-N. kamtschatica* Chronozone.

PALEOMAGNETISM

Procedures

At Sites 885 and 886, pass-through measurements were performed on all APC cores from Holes 885A, 886A, 886B, and 886C. For one to three sections from each core of all holes, both the natural remanent magnetization (NRM) and the remanence after alternating field (AF) demagnetization at 15 mT were measured at a sample spacing of 10 cm. For the other sections, only the demagnetized remanence at 15 mT was measured. Two 7-cm^3 samples were taken from all sections of Hole 885A and one 7-cm^3 sample was taken from all sections of the other holes. Measurements were performed on all samples from Hole 885A using both the Molspin and the Japanese spinner magnetometers. The samples were demagnetized in six steps up to 40 mT. In addition to the NRM demagnetization, the Japanese instrument provided anhysteretic remanent magnetization (ARM) data. The multishot orientation devices were deployed in the lower parts of Holes 885A, 886B, and 886C, and orientations were obtained for Cores 145-885A-6H to -7H, 145-886B-4H to -8X, and 145-886C-4H. Where both the multishot and tensor tools were used, orientations from the two devices agree to within 3°. Automated susceptibilities were measured at 5-cm intervals in whole cores for all of the cores, in conjunction with other measurements performed with the multisensor track.

Results

Pass-through measurements of the remanence after 15-mT demagnetization were shown in Figure 7 for all holes of Sites 885 and 886. These remanence intensities are high enough to measure, except in the middle part of these sequences. Mean intensities after demagnetization are about 20 mA/m from 0 to 23 mbsf (varying between 3 and 40 mA/m), less than 1 mA/m from 23 to 30 mbsf, and 10 mA/m (varying between 1 and 30 mA/m) from 30 mbsf to the bottom.

Whole-core susceptibility measurements and inclination results for Holes 885A, 886B, and 886C (Fig. 8) show similar changes in each hole, and it seems possible to correlate among them. Dashed lines in the figure indicate intercore stratigraphic correlations based on the susceptibility peaks. Inclination results do not show a consistent variation among holes, although Holes 885A and 886A (short hole) seem to be suitable for magnetostratigraphic interpretation.

Figure 9 shows composite plots of discrete sample and pass-through measurements of Hole 885A, as well as typical Zijderveld diagrams. Stepwise demagnetization results for samples indicate that the sequence has mostly a stable single component remanence above a 10 mT coercive force. Samples from the middle part of the low intensity zone (from 23 to 30 mbsf), however, show scattered results that indicate the inability to get a reliable direction reading on the shipboard spinner magnetometer. For the most part, inclination results from pass-through measurements show a change coherent with results from discrete samples, using linear regression fitting demagnetization data from 10 to 40 mT, except for intervals associated with the Brunhes/Matuyama and Gauss/Gilbert boundaries (3.5–4 mbsf and 17–18.5 mbsf, respectively).

Measurements of ARM demagnetization performed using the Japanese spinner magnetometer are also shown with the NRM intensities in Figure 9. Above 23 and below 30 mbsf, the ARM (imparted in 40-mT AF and 0.03-mT DC fields) is in the range of 10^{-4} kA/m (an order of magnitude greater than the NRM). In the middle part of the hole, the ARM is about two orders of magnitude weaker (10^{-6} kA/m). The ARM varies in a similar fashion to the NRM, although the ARM proportion with respect to the NRM is slightly higher toward the base of the section. This result indicates that the grain size distribution of magnetic minerals becomes coarser with depth down the core.

Discussion

The whole-core magnetic record of Hole 885A does not contain short reversal events, because of the low sedimentation rate on the

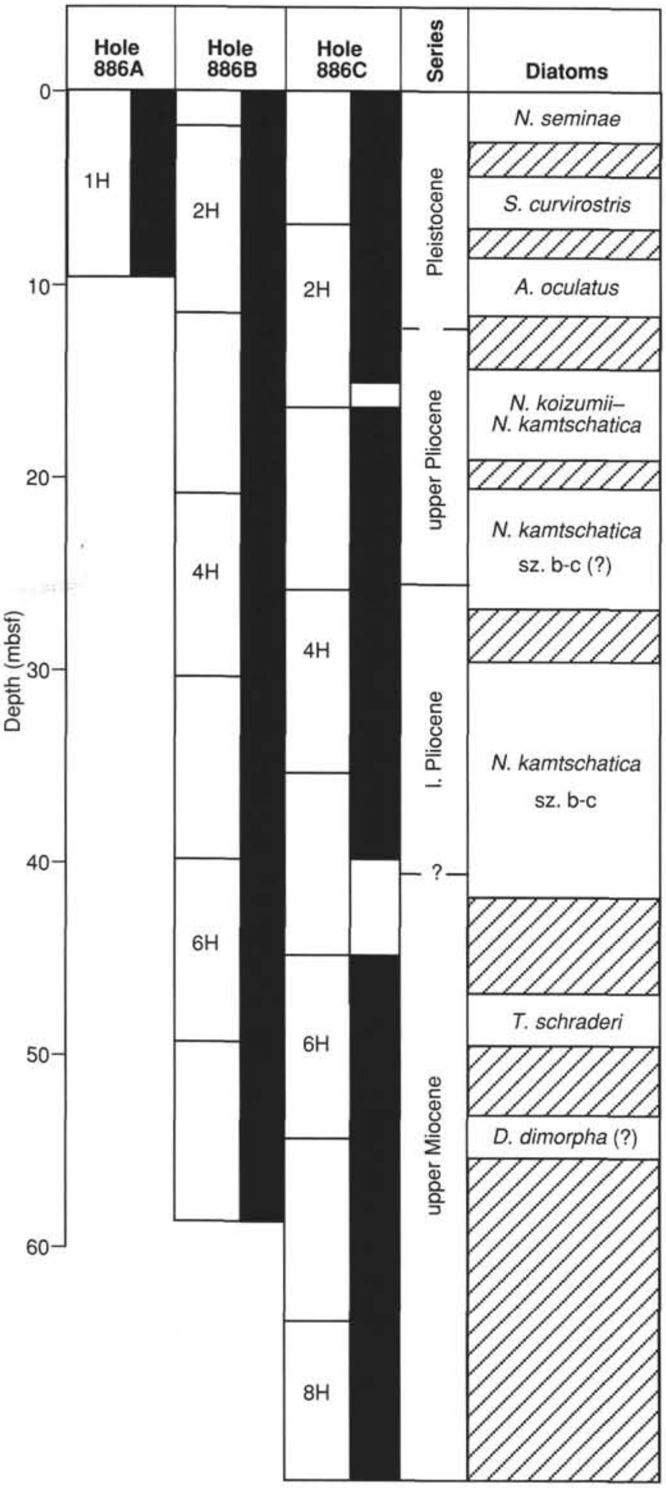

Figure 6. Stratigraphic position of cores, recovery (black), ages, and placement of diatom zones in Holes 886A, 886B, and 886C. Intervals filled by slanted lines indicate uncertainty in the placement of biostratigraphic boundaries.

order of 5 m/m.y. The record shows changes inconsistent with the results from discrete samples taken at the proposed Brunhes/Matuyama and Gauss/Gilbert boundaries. To define the depth of the Brunhes/Matuyama boundary in Hole 885A, the Hole 886A inclination record was referenced on the basis of whole-core susceptibility measurements (Fig. 10), because Hole 886A seems to have the best record for the last 2 Ma at Sites 885/886. The susceptibility measurements vary in a similar manner and can be correlated between these holes; the Brunhes/Matuyama boundary of Hole 885A was defined at 3.95 mbsf. For the Gauss/Gilbert boundary, sample demagnetization results were used, with definition at 17.5 mbsf in Hole 885A. Below this horizon, the whole-core record shows a consistent agreement with individual sample results, except within the low remanence interval.

Hole 885A magnetostratigraphy based on all the data refers to the time scale of Cande and Kent (1992), as shown in Figure 11. The ages and depths of these reversal boundaries are listed in Table 5 for all holes at Sites 885/886.

SEDIMENTATION RATES AND FLUXES

Sedimentation Rates

To calculate sedimentation rates and sediment fluxes (mass accumulation rates), we considered Sites 885 and 886 to be one site with two time-stratigraphic intervals equivalent to lithologic Units I and II. As illustrated in Figure 12, the unit boundaries at these sites differ in depth below seafloor by about 10 m (see also Table 2). For convenience in averaging data, we have defined the two time-stratigraphic units at ~17 and ~52 m, at the Unit I and Unit II boundaries of Hole 886C. The age-depth relationship is a composite based on magnetostratigraphy above ~52 mbsf, because different reversals were recovered at the various holes and because linear rates of sedimentation differ between the sites. Below that level, in lithologic Unit III, neither reliable magnetostratigraphy nor biostratigraphy is available at this time. Considering the slightly different age-depth relationships for each of these sites, it is possible to fit the data with an average linear rate of sedimentation of 5.65 m/m.y. for lithologic Units I and II (shown as a dashed line in Fig. 12). It is important to stress that our estimated rates of sedimentation reflect averages for intervals of time spanning millions of years. Significant variability is likely within these intervals, which might drive large changes in MAR on shorter time scales. For example, both Holes 885A and 886C show evidence of sharply decreased sedimentation rates or a hiatus at about 8 Ma (Fig. 12).

Sediment Fluxes

Sediment fluxes were determined in the conventional way, taking the product of the sedimentation rate, the dry-bulk density, and the concentration of the sediment component. Dry-bulk density values were taken from pycnometer measurements at all sites, and sedimentary component data came from smear slide estimates at all sites, with the exception of percentages of carbonate and total organic carbon (TOC), both of which were measured analytically at Hole 886B. Raw data for each of the two time-stratigraphic intervals at Sites 885/886 were averaged and are presented in Table 6. Average fluxes (in $g/[cm^2 \cdot k.y.]^{-1}$) were calculated for the two upper units, but only clay and diatom fluxes are significantly different from zero; all results are listed in Table 6. These results are only semi-quantitative, because of the nature of estimates of smear slide abundances, as well as errors associated with assuming a model sedimentation rate and averaging data from different sites.

Despite these limitations, the principal change in flux patterns that we were able to distinguish at Sites 885/886 occurred during the middle Pliocene about 3 m.y. ago. That age estimate results from using an average sedimentation rate for three different cores and a fixed unit boundary. For example, if the Unit I/Unit II contact for these site is fixed at ~17 m, then boundary ages range from ~2.6 Ma at Holes 886B and 886C to ~3.6 Ma at Hole 885A. For the interval from ~3 to ~9 Ma, sedimentation was dominated by relatively high diatom (0.2 $g[cm^2 \cdot k.y.]^{-1}$) and low clay (0.03 $g[cm^2 \cdot k.y.]^{-1}$) fluxes. In contrast, this dominance switched in younger sediments to a reduced diatom flux (0.2 $g[cm^2 \cdot k.y.]^{-1}$) and an increased clay flux (0.18 $g[cm^2 \cdot k.y.]^{-1}$). This change was relatively sudden and is distinctive enough to define separate sedimentary units. More concentrated study of single holes probably will show that the change occurred near 2.6 Ma. In general,

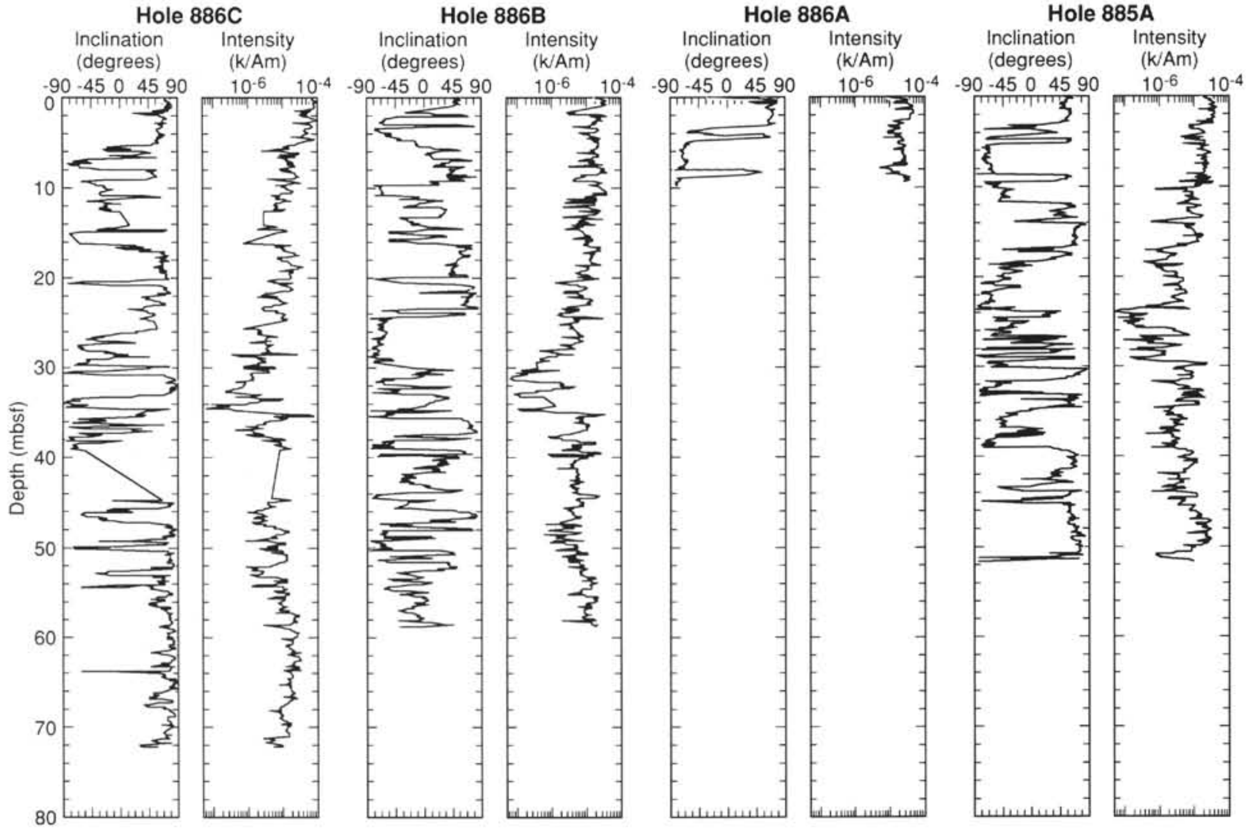

Figure 7. NRM intensities, after demagnetization at 15 mT, and inclinations from Holes 885A, 886A, 886B, and 886C.

this pattern of change is consistent with other Leg 145 sites to the west. On Detroit Seamount (Sites 882 through 884) maximum diatom flux also occurs in lower Pliocene and upper Miocene sediments. Clay fluxes at Sites 885/886 are about a factor of 10 lower than at other Leg 145 sites, but are consistent with fluxes of eolian dust measured in the North Pacific Ocean red clay province (Rea et al., 1985).

INORGANIC GEOCHEMISTRY

Eleven interstitial-water samples were collected at Site 886 at depths ranging from 1.45 to 55.75 mbsf. Four closely spaced samples were taken from Hole 886A between 3.45 and 7.95 mbsf, and seven broadly spaced samples were collected from Hole 886B at depths ranging from 1.65 mbsf to near the bottom of the hole at 55.75 mbsf. The samples from Hole 886A were assigned to the depth scale for Hole 886B by correlating the magnetic susceptibility profiles for the two holes. Analytical results are listed in Table 7 and have been plotted separately for the two sample sets on all graphs in this section.

The pore-water samples span all of lithologic Units I (0–17.3 mbsf), II (17.3–50.3 mbsf), and much of Unit III (50.3–71.9 mbsf), which are composed of clay with spicules, diatom clay and diatom ooze with clay, and dark grayish-brown clay, respectively (see "Lithostratigraphy" section, this chapter).

Chloride concentrations in interstitial waters at Site 886 range from the North Pacific Ocean Deep-Water value (~555 mM) in the shallowest sample (1.45 mbsf; Fig. 13A) to a maximum of ~564 mM at 26.75 mbsf. As at Sites 881 through 884, the Cl^- maximum probably reflects the ongoing diffusive adjustment of the pore-water Cl^- distribution to the increased mean salinity of seawater during glacially dominated Pleistocene time and the fresher seawater of the Holocene (McDuff, 1985). The depth of the Cl^- maximum at Site 886 is similar to that normally encountered in pelagic sections (McDuff, 1985). Below 26 mbsf, the chloride content declines slightly to the bottom at 55 mbsf.

Nitrite was undetected in the four samples from Hole 886A and in the upper three pore-water samples in Hole 886B. It was not measured in the remaining samples.

The dissolved manganese concentrations in the shallowest samples at Site 886 (~2–5 µM at 1.45 to 1.65 mbsf) are significantly higher than in the overlying Pacific Ocean Bottom Water (<100 nM in seawater; Landing and Bruland, 1980; Fig. 13B). Concentrations continue to increase to a shallow subsurface maximum of 28.4 µM at ~27 mbsf, reflecting reductive dissolution of Mn oxides in the sediment column. Downward and upward diffusion from the maximum is implied by the profile. This probably reflects the nonsteady-state depositional history at this site, where Oligocene oxidizing clays (lithologic Unit III) were buried by upper Miocene–Pliocene diatom ooze (lithologic Unit II). A higher oxidant demand in the latter is implied by the occurrence of the reduced manganese maximum in the pore waters.

Titration alkalinity remains relatively low (from 2.49 to 2.74 mM) in the pore waters at Site 886 (Fig. 13C), as does the sulfate concentration, which is almost identical throughout the section to that in North Pacific Ocean Deep Water (Fig. 13C). The sulfate and alkalinity data jointly confirm that little sulfate reduction is occurring in the top 55 mbsf at this location. The oxidant demand appears to be satisfied by the manganese and iron oxyhydroxides presumed to be present in this interval; these phases would act as the thermodynamically preferred electron acceptors.

Dissolved ammonium in pore waters at Site 886 was not detected in samples from the upper 17 mbsf of the section (Fig. 13D). Between this depth and ~36 mbsf, the ammonium concentration increases to 154 µM, then decreases to 70 µM at 55 mbsf (Fig. 13D). The ammonium represents a diagenetic product of organic matter degradation

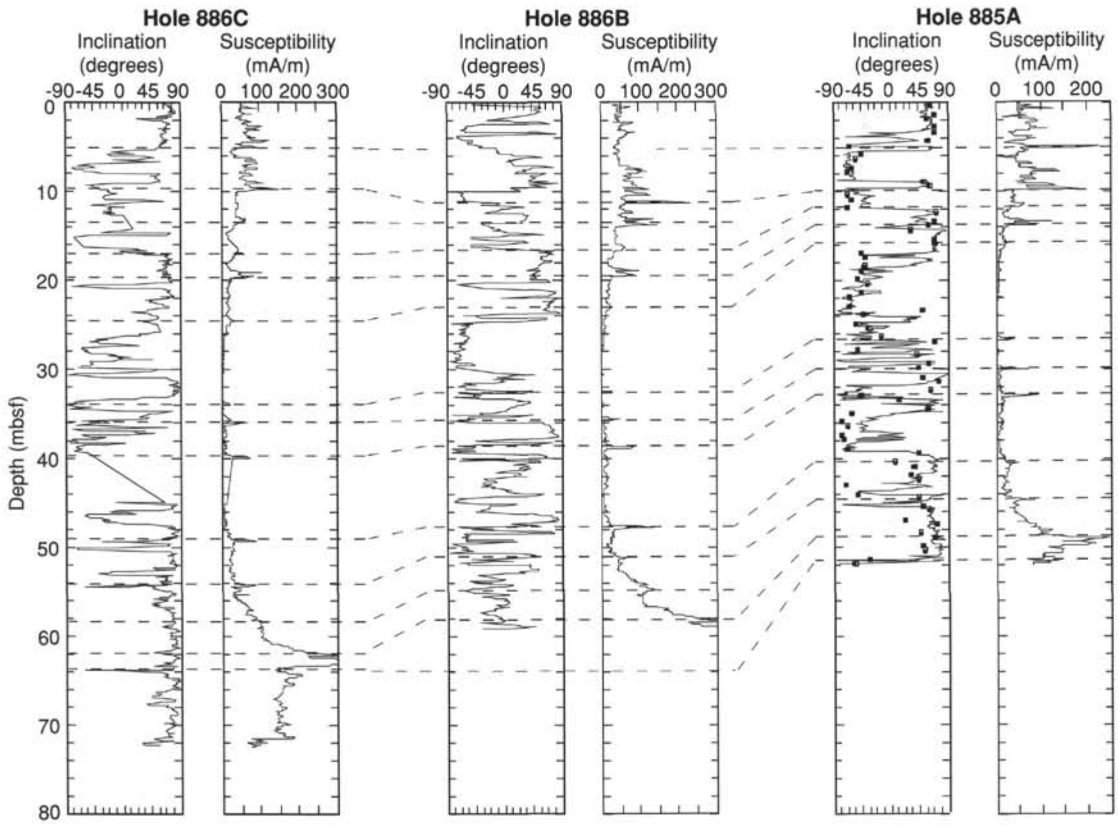

Figure 8. Whole-core susceptibility and magnetic inclination records, after 15-mT demagnetization, from Holes 885A, 886B, and 886C. Dashed lines indicate stratigraphic correlations based on the susceptibility peaks.

presumably accomplished through nitrate and manganese and/or iron oxyhydroxide reduction, rather than sulfate reduction.

The magnesium concentrations in all of the samples are similar to those in North Pacific Ocean Deep Water (ranging from 51.7 to 54.0 mM) and exhibit little variation with depth (Fig. 14A). Similarly, calcium concentrations throughout the sampled section are about the same as those in North Pacific Ocean Deep Water (10.6 mM; Fig. 14A). The Mg and Ca data suggest that diffusive exchange with overlying seawater dominates the distribution of these elements. Alteration of basaltic basement appears to have had little effect on the profiles. These observations are consistent with the existence of a very thin sedimentary cover at Site 886.

The dissolved silicate concentrations in the uppermost pore-water samples at Site 886 (~551–583 μM) are sharply higher than in the overlying North Pacific Ocean Bottom Water (~160 μM), reflecting pronounced dissolution of opaline diatom frustules within the uppermost sediment column (Fig. 14B), as observed previously at Sites 881 through 884. The average silicate concentration generally increases with depth to a maximum of ~800 μM at ~36 mbsf, which is the center of lithologic Unit II (diatom ooze). The silicate concentration decreases from 800 to about 698 μM between about 36 and 55 mbsf. The dissolved silicate maximum between 26 and 36 mbsf is coincident with an increase in diatom abundance (see "Biostratigraphy" section, this chapter, for a discussion).

The strontium concentration in the uppermost pore-water sample is slightly higher than that in modern North Pacific Ocean Deep Water (92–94 compared with 87 μM; Fig. 14C) for reasons that are unclear. The Sr^{2+} content remains essentially constant throughout the measured section, with a small increase at 45 mbsf to 99 μM and a decrease to 88 μM at 55 mbsf. The latter may reflect the change in lithology from diatom ooze of Unit II to clay in Unit III.

Lithium concentrations in the shallowest samples at Site 886 are slightly higher than those of North Pacific Ocean Deep Water (28.3–31.5 μM compared with 26.8 μM in seawater; Fig. 14C). The profile shows little variation with depth to 55 mbsf at this site.

Sodium (calculated by charge balance) shows little variation in the pore waters down the core; the concentration in the uppermost sample is equal to that of North Pacific Ocean Deep Water (476 mM; Fig. 14D). A slight increase in sodium, coincident with the chloride maximum, occurs between 17 and 26 mbsf (Table 7), reflecting the Quaternary salinity effect discussed earlier.

The concentration of potassium in the surface samples (10.86–11.31 mM) is roughly the same as that in North Pacific Ocean Deep Water (10.35 mM) and remains approximately constant to the base of the section (Fig. 14D). As for Mg and Ca, no evidence exists that alteration reactions in the underlying basalt have influenced the pore-water distribution of Sr, Li, Na, or K at this location. Given that the basalt fragments recovered at the base of Holes 885A and 886B showed evidence of extensive alteration (see "Igneous Petrology" section, this chapter), we can conclude that diffusive exchange with overlying seawater throughout the drilled section is facilitated by the high porosity of the sediments and thin sedimentary cover at this location. Such exchange probably dominates the pore-water chemistry, rather than diagenetic chemical reactions in the underlying volcanic basement.

ORGANIC GEOCHEMISTRY

Volatile Hydrocarbons

As required by safety and pollution considerations, real-time monitoring of the volatile hydrocarbons was performed on sediments of Sites 885 and 886. Twenty samples were collected using the headspace

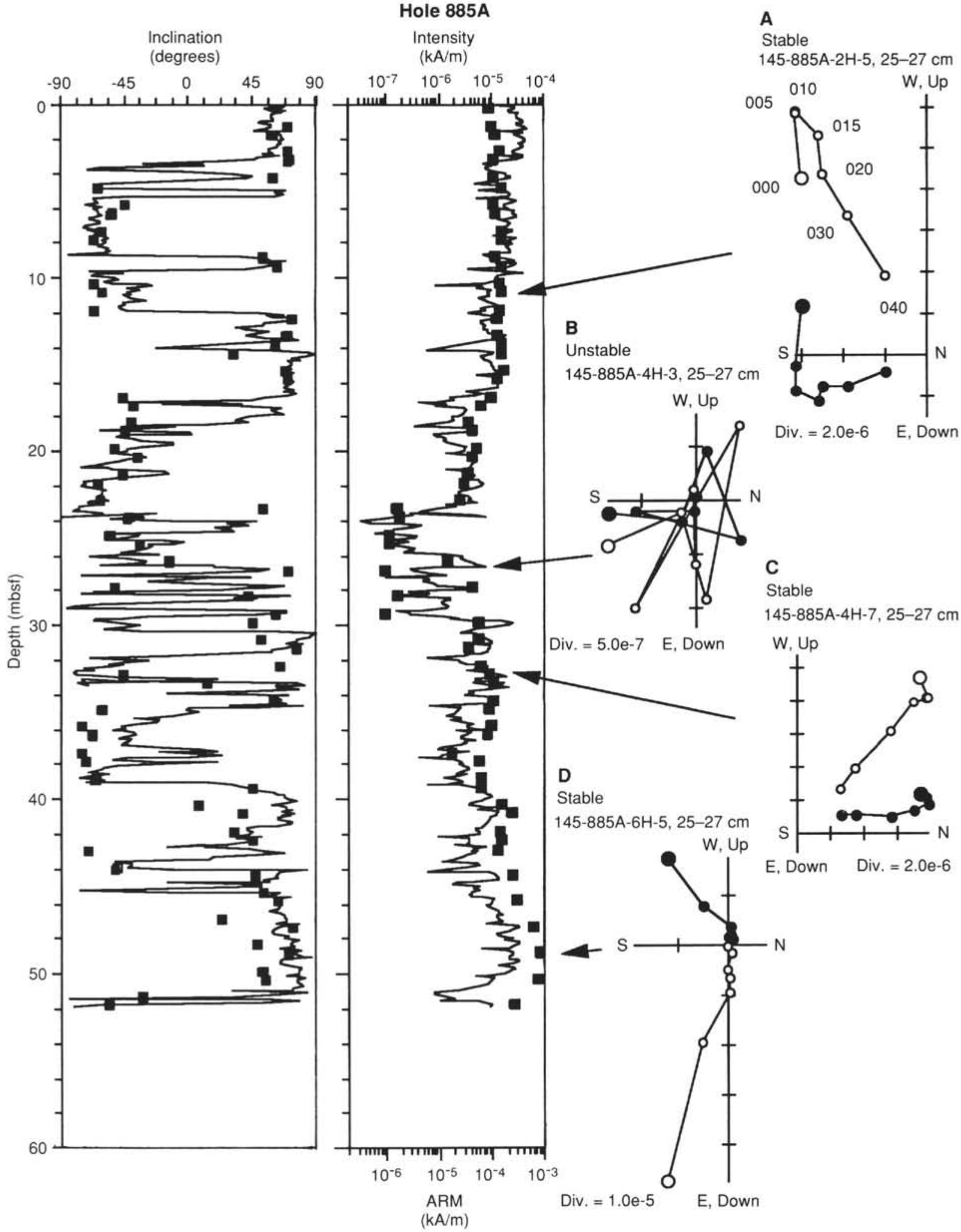

Figure 9. Comparison of results from Hole 885A whole-core measurements of NRM demagnetized at 15 mT (solid line) with linear regression results from discrete samples, using demagnetized data from 10 to 40 mT (solid square). Center figure shows comparison of the whole-core demagnetized NRM intensity with sample ARM given in 40-mT AF and 0.03-mT DC fields for the same hole. Examples of Zijderveld plots are shown for samples presented as open circles on Up-SN section and as solid circles on WE-SN section. **A**, **B**, **D.** Stable behavior. **C.** Unstable behavior, thought to be responsible for scattering results in the whole-core result.

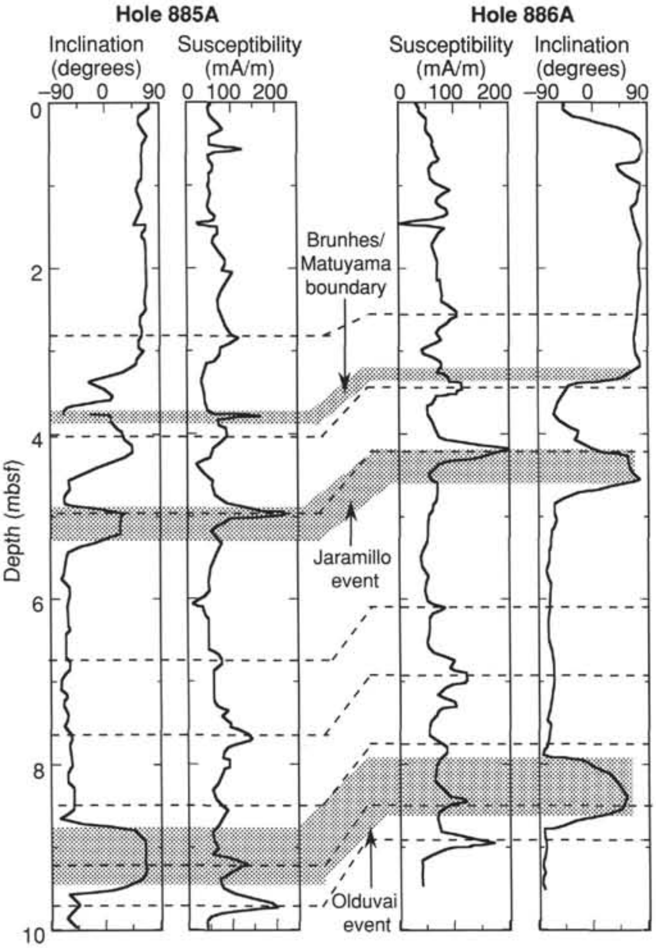

Figure 10. Comparison of results from whole-core susceptibility measurements and magnetic inclination records between Hole 886A and top 10 m of Hole 885A. Dashed lines indicate stratigraphic correlations base on the susceptibility peaks.

technique (see "Organic Geochemistry" section in the "Explanatory Notes" chapter, this volume) and measured in a Carle gas chromatograph. The results from both sites are presented in Tables 8 and 9. The methane (C_1) concentration did not exceed 5 ppm, and ethane (C_2) and propane (C_3) could not be detected in samples from these sites.

Carbonate Carbon

Inorganic carbon (IC) was determined on 37 and 39 samples gathered from Sites 885 and 886, respectively, using a Coulometrics carbon dioxide coulometer. However, no IC (and thus no $CaCO_3$) was detected in the sediments, because these sites were positioned well below the calcium carbonate compensation depth (CCD) in a water depth of more than 5700 m.

Organic Carbon

Total carbon (TC) was measured on the same samples used for the coulometer, by means of a Carlo Erba NCS analyzer. Because no carbonate is present in the sediments of Sites 885 and 886, one can assume that TC equals the amount of total organic carbon (TOC). Total nitrogen (TN) values were near or below the detection limit of the NCS analyzer. The results of the TC and TN measurements are presented in Tables 10 and 11 and plotted vs. depth in Figures 15 and 16.

The TOC concentrations in the sediments of Sites 885 and 886 are very low, ranging between 0.02% and 0.25%. Except for one interval that shows slightly higher TOC values (25–31 mbsf in Site 886), no clear trend or correlation to the lithologic units (see "Lithostratigraphy" section, this chapter) can be seen in the data. This finding indicates that almost all of the organic carbon produced in the surface waters was subjected to oxic degradation in the water column and in the sediments. The latter conclusion is supported by the brownish color of the sediment and by the absence of sulfate-reducing conditions in the sediments (see "Inorganic Geochemistry" section, this chapter).

PHYSICAL PROPERTIES

Introduction

Index property (densities, porosities, water contents, and void ratios), digital sediment velocimeter (DSV), and shear strength measurements were performed at approximately 150-cm intervals in cores from Holes 885A, 886B, and 886C (Table 12). Index properties and shear strength were measured at 150-cm intervals in the single core recovered from Hole 886A. Thermal conductivity was measured at 3-m intervals in cores from Holes 885A, 886B, and 886C. Continuous measurements of GRAPE bulk density, P-wave velocity, and magnetic susceptibility were performed on cores from all four holes. Tables containing the compressional wave velocity and thermal conductivity data from Holes 885A, 886B, and 886C are included here, as are tables of index property and shear strength data from Holes 885A, 886A, 886B, and 886C (Tables 13 through 22). To improve the legibility of the downhole profiles, while reducing the resolution as little as possible, GRAPE data have been smoothed using a 29-point moving average, whereas data from the P-wave logger (PWL) were filtered to remove data points associated with low signal strengths, then smoothed using a five-point moving average. All other data are presented in original form.

Index Properties and Vane Shear Strength

Shear strength in cores from Holes 886B and 886C increases in a roughly linear fashion downhole from a value of approximately 10 to a value of 50 g/cm^3 at a depth of 60 mbsf (Figs. 17 through 19). This trend reflects an increasing degree of consolidation with depth, as might be expected in an area characterized by a low sedimentation rate, and thus, adequate time for drainage of the sediment during burial. However, the shear strength profile for Hole 885A (Fig. 17) indicates a sharp increase in shear strength from approximately 20 to 100 g/cm^3 between 20 and 26 mbsf. This increase does not appear to occur in either Hole 886B or 886C. Bryant et al. (1986) used an empirical relationship between the undrained shear strength (S_u) and effective overburden pressure (P_o') (Skempton, 1970) to infer the state of consolidation in the sediment column. Application of this technique to the data from Holes 885A, 886B, and 886C produced the profiles of S_u/P_o' vs. depth for Holes 885A, 886B, and 886C, presented in Figure 20. The vertical line at an S_u/P_o' value of 0.22 has been included in the plots to distinguish the underconsolidated zone (S_u/P_o' <0.22) from the normally to overconsolidated zone (S_u/P_o' >0.22). The profiles are fairly typical for unconsolidated marine sediments in that the uppermost part of the section in all three holes is apparently normally to overconsolidated (S_u/P_o' >0.22), whereas the sediment below approximately 10 mbsf appears to be underconsolidated, with the exception of the peak in shear strength at 20 mbsf in Hole 885A. This peak value is indicative of a zone of normally to overconsolidated sediment in an otherwise underconsolidated portion of the sediment column and may indicate the existence of an erosional or nondepositional unconformity at this depth in Hole 885A. An unconformity might account for some of the variation in the thickness of the section seen in the lithostratigraphic correlations of Holes 885A, 886B, and 886C (see "Lithostratigraphy" section, this chapter). Alternatively, cementation may be responsible for this zone of relative overconsolidation, but this is deemed unlikely.

Downhole profiles of wet-bulk density, dry porosity, dry water content, dry-bulk density, and grain density clearly reflect the litho-

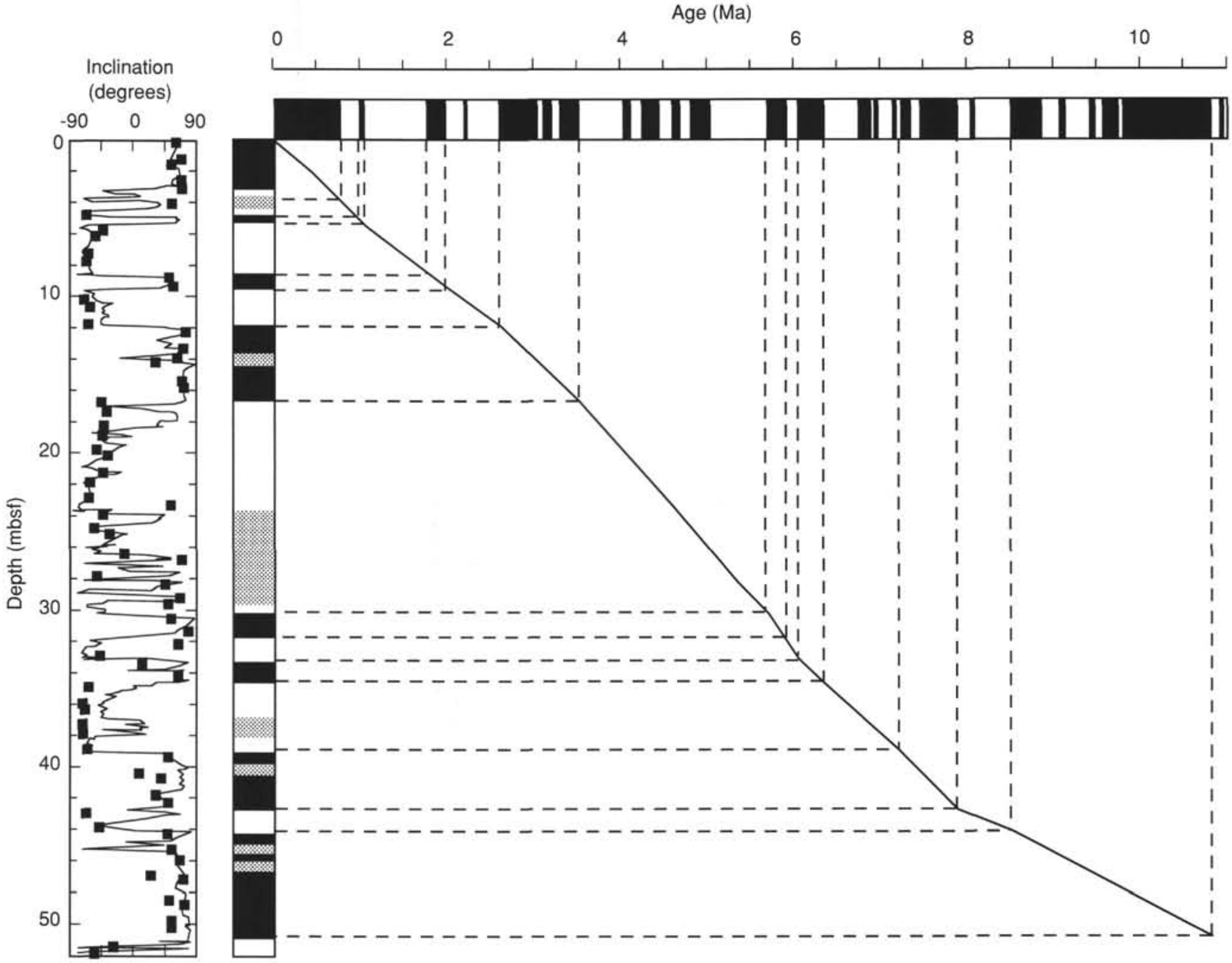

Figure 11. Interpretation diagram of magnetostratigraphy for Hole 885A, using the time scale of Cande and Kent (1992).

logic changes associated with the three upper lithostratigraphic units defined for the section (see "Lithostratigraphy" section, this chapter). Correlation of the index property data from Holes 885A, 886B, and 886C also suggests a thickening or thinning of the upper three lithostratigraphic units; the thinnest section occurs in Hole 885A and the thickest in Hole 886C (Figs. 17 through 19, 21, and 22).

The clay-rich intervals, lithologic Units I and III, are characterized by average wet-bulk density, dry-bulk density, and grain density values of 1.32, 0.5, and 2.50 g/cm^3, respectively, with Unit III having slightly higher values than Unit I. The dry porosity and dry water content values in Unit I remain fairly constant, with values averaging 80% and 190%, respectively. In lithologic Unit II, dry porosity and dry water content increase slightly, coincident with a sharp decrease in dry-bulk density, which is consistent with a lithology of >90% biogenic silica. The top of Unit III is marked by a sharp decrease in dry porosity and dry water content values (to 80% and 140%, respectively), and a sharp increase in wet-bulk density, dry-bulk density, and grain density (to 1.33, 0.5, and 2.6 g/cm^3, respectively). The trend reflected in the index property profiles suggests a gradational contact between Units I and II and a sharp contact between Units II and III.

The grain density profiles show a sharp increase to values of approximately 3.1 g/cm^3 in the data from the last core from each hole. These unusually high values may be the result of an overestimation of the dry volume because of the extremely fine-grained nature of the sediment in this interval or possibly may reflect the presence of basalt or heavy metal grains. An XRD examination of the sediment revealed the presence of the mineral apatite, a common accessory mineral in igneous rock assemblages (Deer et al., 1966). A combination of the two is the most likely explanation.

GRAPE Data

Although the GRAPE bulk density values were consistently higher by approximately 0.1 g/cm^3 than those obtained from pycnometer analysis, the GRAPE bulk density trends from all four holes drilled at Site 885/886 (Figs. 17 through 19) paralleled those obtained with the helium pycnometer. The GRAPE analyses are performed on sealed whole-core sections, whereas the pycnometer analyses are performed on discrete samples removed from the core. It is unlikely that this offset is the result of a calibration error, because the GRAPE data from Site 884 (see "Physical Properties" section, "Site 884" chapter, this volume) show that the profiles tend to converge with increasing induration. The offset between the two data sets is more likely the result of post-splitting sediment expansion (see "Physical Properties" section, "Site 881" chapter, this volume).

Compressional Wave Velocities

Both the DSV and the P-wave logger yielded average P-wave velocity values of approximately 1500 m/s for the entire section in

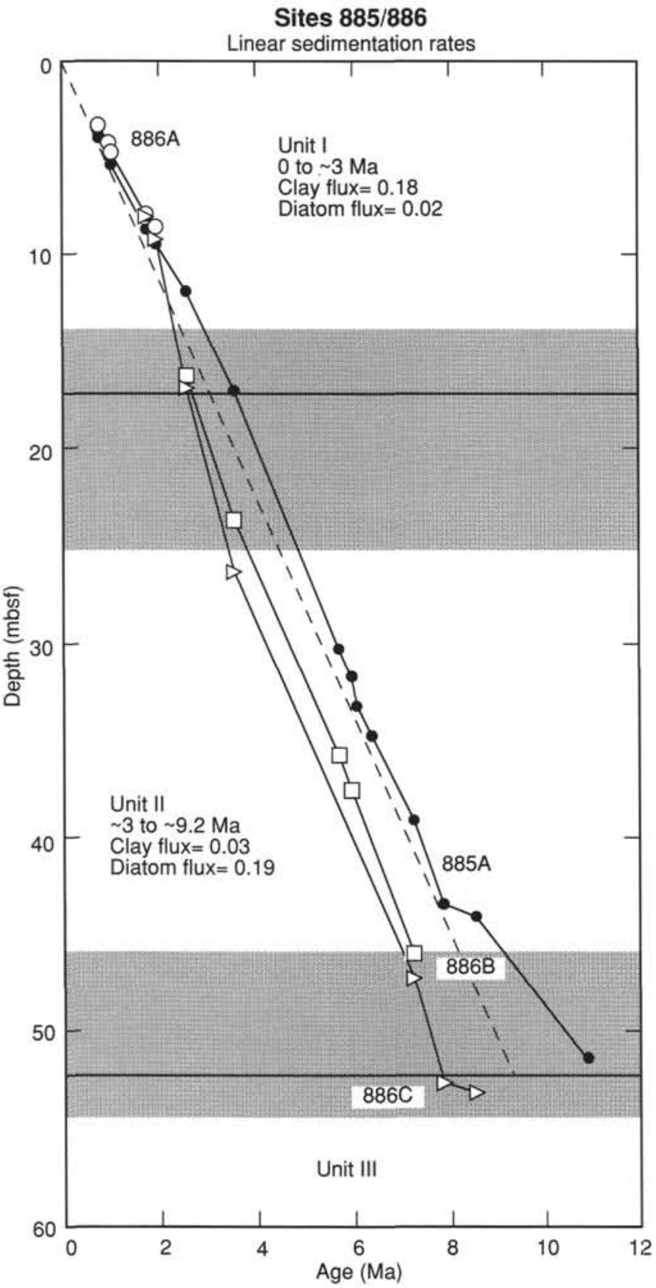

Figure 12. Plot of sedimentation rate for Sites 885/886 using magnetostratigraphy. Dashed line shows model sedimentation rate used for flux calculations, shaded pattern shows range of unit boundary locations among these sites, and average unit boundaries are assumed to occur at ~17 and ~52 mbsf (solid lines). Average rates and fluxes (in g[$cm^2 \cdot$ k.y.]$^{-1}$) have been calculated for the upper two lithologic units, but no chronostratigraphy is now present below Unit II. The major flux change at this site occurs at the lithologic Unit I/Unit II boundary with a change from dominantly diatomaceous sediments to dominantly clayey sediments. That level in these cores probably marks the onset of Northern Hemisphere glaciation at ~2.6 Ma.

Hole 885A and approximately 1515 m/s for the entire section in Holes 886B and 886C (Fig. 23). The spiky nature of the P-wave logger data may be attributed to the presence of ferro-manganese nodules (see "Lithostratigraphy" section, this chapter) or low signal strength. The DSV profiles do not reflect the abundance of the nodules because of the bias inherent in the noncontinuous sampling for DSV testing. P-wave velocity in unconsolidated sediments typically varies directly with wet-bulk density and inversely with porosity. Figure 24 reveals a weak correlation between P-wave velocity and porosity in the samples from Unit III. The P-wave velocities measured in samples from lithologic Units I and II do not appear to be a function of porosity, which remains consistently high (>80%), but of lithology. Consequently, changes in lithology are the dominant cause of P-wave variations in Units I and II.

Thermal Conductivity

Thermal conductivity values in Units I and II decrease from mud-line values of 1.0 W/(m·°C) in Hole 885A and 1.1 W/(m·°C) in Holes 886B and 886C to values approaching 0.75 W/(m·°C) near the base of Unit II (Fig. 25). A marked increase in thermal conductivity to values >1.0 W/(m·°C) occurs at the top of Unit III. Figure 26 shows a weak correlation between porosity and thermal conductivity. The exceptionally high porosity in all three units appears to be the dominant factor controlling the thermal conductivity and probably acts to mask the effect of lithology on thermal conductivity.

SEISMIC-LITHOLOGIC CORRELATION

All the Leg 145 drilling locations were surveyed in order to drop the beacon at the proper pre-selected location. In every case, the surveys were run in the figure of the number 4 with the long leg duplicating the site-survey track line used to select the site and the cross-leg being as nearly orthogonal as practical. The shipboard air-gun seismic reflection profiling system was used for all the surveys except for that at Site 883, when it was inoperable; the 3.5-kHz profiling system was used to locate that drill site. Details of the surveying and seismic processing techniques are given in the "Site 881" chapter ("Seismic-Lithologic Correlation" section, this volume).

Sites 885 and 886 are located in lenses of sediment about 2.2 km apart, each less than 0.1 s thick (Figs. 27 and 28). At Sites 885 and 886 acoustic basement is altered basalt, rather than the expected limestone. Lithologic Unit III, which is brown pelagic clay, overlies basement and is separated from the above units by a more prominent reflector. Unit II, diatom ooze, and lithologic Unit I, siliceous clay, are not readily distinguishable in the profiles.

SUMMARY AND CONCLUSIONS

Geological Record

At Sites 885 and 886, located 2.2 km apart, we recovered about 70 m of sediments and 0.6 m of underlying basalts. The sedimentary sequence penetrated at both sites displays similar composition and succession down the section, but differs in thickness, being 52 m thick at Site 885 and 71.9 m thick at Site 886. Three lithostratigraphic units can be recognized at both sites.

Unit I (0–17.3 mbsf) is Quaternary to late Pliocene in age and consists of reddish-brown and brown pelagic clay in concentrations that typically range from 65% to 95%. Diatoms and sponge spicules constitute the minor lithologies of this unit. Diatom concentrations are relatively constant, making up 4% to 15% of the section. Spicule concentrations are low (1% to 15%) in the upper half of the unit and increase to 25% to 30% in the lower part. Volcanic ash and pyrite are present as accessory lithologies. Volcanic ashes form two thin (1 and 3 cm) but distinct layers with sharp lower and gradational upper boundaries in the middle of the unit at Site 885, but such layers were not observed at Site 886, probably because these were obscured by bioturbation. Pyrite is scattered throughout the upper portion of the unit either in the form of concretions about 2 cm in diameter with limonite surface staining and aggregated clots, or intergranular cement in ash-filled burrows. The sediment is bioturbated throughout the unit and exhibits dark-colored burrows and mottles and light-colored pockets filled with ash and spicule oozes.

Unit II (17.3–50.3 mbsf) is of late Pliocene to late Miocene age and consists of light brown to yellowish-brown diatom ooze having diatom

Table 5. Depths of polarity chron boundaries in Holes 885A, 886A, 886B, and 886C.

Polarity chron	Depth (mbsf) Hole 885A	Hole 886A	Hole 886B	Hole 886C	Age (Ma) (CK 92)[a]
Brunhes/Matuyama	3.95 (1H-3, 95 cm)	3.38 (1H-3, 48 cm)			0.780
Termination Jaramillo	4.95 (2H-1, 35 cm)	4.21 (1H-3, 121 cm)			0.984
Onset Jaramillo	5.36 (2H-1, 76 cm)	4.71 (1H-4, 21 cm)			1.049
Termination Olduvai	8.77 (2H-3, 110 cm)	8.00 (1H-6, 50 cm)		8.03 (2H-1, 123 cm)	1.757
Onset Olduvai	9.54 (2H-4, 34 cm)	8.66 (1H-6, 116 cm)		9.18 (2H-2, 88 cm)	1.983
Matuyama/Gauss	11.95 (2H-5, 145 cm)		16.23 (3H-4, 43 cm)	16.83 (3H-1, 53 cm)	2.600
Gauss/Gilbert	17.05 (3H-2, 145 cm)		23.61 (4H-2, 131 cm)	26.33 (4H-1, 53 cm)	3.553
Termination C3An.1n	30.34 (4H-5, 74 cm)		35.76 (5H-4, 96 cm)		5.705
Onset C3An.1n	31.76 (4H-6, 66 cm)		37.62 (5H-5, 132 cm)		5.946
Termination C3An.2n	33.24 (5H-1, 14 cm)				6.078
Onset C3An.2n	34.80 (5H-2, 20 cm)				6.376
Termination C4n.1n	39.10 (5H-5, 0 cm)		45.96 (6H-5, 16 cm)	47.28 (6H-2, 98 cm)	7.245
Onset C4n.2n	43.50 (6H-1, 90 cm)			52.65 (6H-6, 35 cm)	7.892
Termination C4An	44.10 (6H-2, 0 cm)			53.12 (6H-6, 82 cm)	8.529
Onset C5n.2n	51.33 (6H-6, 123 cm)				10.834

[a] Cande and Kent (1992) geomagnetic polarity time scale.

concentrations ranging from 55% to 95% and averaging 80%. A dark yellowish-brown clayey diatom ooze from approximately 49 mbsf to the base of Unit II at 50.3 mbsf is a transitional subunit between the diatom ooze and the underlying clayey unit. Ash, pumice clasts, limonite, and ferro-manganese nodules and nodule fragments compose minor lithologies, particularly in the lower portion. Ashes form a single distinct layer in the middle of the unit and also occur scattered throughout the section as burrow fillings. The ferro-manganese nodules are black or dark brown and botryoidal in shape; the largest of these are 6 to 8 cm along the major axis and typically have distinct concentric internal structure with volcanic(?) clasts as cores. Sediments display slight bioturbation, as indicated by burrows, mottles, and pockets.

Unit III (50.3–71.9 mbsf in Hole 886C) is late Miocene in age in the uppermost part and undated down throughout most of the sequence, being barren of any fossils except the fish teeth in the deeper portion. This unit is composed predominantly of brown to dark brown pelagic clay that grades down to dark reddish-brown hematitic clay at the base of the unit. The uppermost part contains up to 20% diatoms. The characteristic feature of this unit is a high concentration (10%–30%) of authigenic and/or diagenetic minerals including zeolite, hematite, and ferro-manganese nodules scattered throughout the section. Co-mingled chert and ferro-manganese oxide concretions (<1 cm in diameter) occur in separate thin (3–5 cm) layers. The color, shape, and internal structure of ferro-manganese nodules are similar to those observed in overlying unit.

Unit IV (52.1–58.8 mbsf in Hole 885A and 68.5–68.9 mbsf in Hole 886B) consists of aphyric basalt pebbles. The basalts are highly altered and have surficial coatings of yellowish, orange, or black alteration products. Some relatively fresh pieces contain extremely rare microphenocrysts of moderately altered plagioclase and olivine completely altered to iddingsite in a microcrystalline groundmass. Two lithologic units can be tentatively recognized based on an altered glassy margin at the top of lower flow in Hole 885A. Because of poor recovery and the extent of alteration, the nature of these basalts remains unknown.

Shipboard measurements of the physical properties are in good agreement with major lithologies. The clay of Unit I is characterized by relatively high dry bulk density (DBD) values varying from 0.4 to 0.55 g/cm^3 (average 0.5 g/cm^3) and by porosities averaging 80%. The diatom ooze of Unit II is more porous (83%) and, accordingly, dry-bulk density values decrease to 0.25 g/cm^3. Dry bulk densities increase to average values of 0.5 g/cm^3, and porosity correspondingly decreases again to 80% in the pelagic clays of Unit III.

Units I and II contain abundant-to-common diatoms of good-to-moderate preservation, providing continuous zonation ranging from the Miocene *Thalassionema schraderi* Zone through the late Pleistocene *Neodenticula seminae* Zone. The assemblage at Sites 885/886, along with diatom zonation from latitudinally close DSDP Leg 86 sites (Koizumi and Tanimura, 1985), provides a link between the equatorial and subarctic North Pacific Ocean. Radiolarians are present throughout these units, but zonation is possible only for the Pleistocene interval. Ichthyoliths are the only fossils present in the pelagic "red" clays of Unit III. Despite the relatively slow sedimentation rates, good paleomagnetic reversal stratigraphy down to Anomaly 3 was obtained both at Sites 885 and 886, providing reliable age control for biostratigraphic zonations. The Matuyama/Gauss reversal boundary is near the boundary between lithologic Units I and II, marking as it does in other Leg 145 sites a distinct transition between two different lithologies.

Linear sedimentation rates (LSR) within the stratigraphical well-constrained portion of the sequence (Units I and II) average 5.7 m/m.y. The LSR did not vary significantly from the late Miocene through Quaternary. Fluxes of clay and diatoms are 0.03 and about 0.2 $g(cm^2 \cdot k.y.)^{-1}$, respectively, in the upper Miocene–upper Pliocene Unit II. Clay flux increases up to 0.18 $g(cm^2 \cdot k.y.)^{-1}$ in the uppermost Pliocene through Quaternary interval, whereas diatom flux decreases to 0.02 $g(cm^2 \cdot k.y.)^{-1}$.

Paleoceanography and Paleoclimatology

Basalt was recovered at both Sites 885 and 886 (52 and 71 mbsf, respectively) at much shallower depths than expected. The seismic record across these sites shows sedimentary cover above acoustic basement that has a thickness of about 75 m, (Figs. 27 and 28) but this acoustic basement was expected to be Cretaceous limestone. The nature and age of these basalts remain unknown, but their presence at this depth in the section emphasizes an unusual history of the seafloor in this area. Were the basalt considered "true" oceanic seafloor, then the thin carbonate cover that generally overlies oceanic basement is absent here. If the basalts are a sill within the sedimentary sequence (note that a baked contact cannot be observed), then volcanic activity has occurred in the region at least several tens of million of years after formation of oceanic seafloor.

The oldest reliably dated sediments at both sites are late Miocene in age. Before that time, pelagic clay deposition dominated the region. The sediment is typical "red" or "brown" clay recovered elsewhere in the North Pacific Ocean (McManus, Burns, et al., 1970; Thiede, Vallier, et al, 1981; Heath, Burckle, et al., 1985; McCoy and Sancetta, 1985; Leinen, 1989). These clays accumulated very slowly at abyssal depths beneath oligotrophic waters and consist of terrigenous, hydrogenous, and hydrothermal minerals (Kadko, 1985; Leinen, 1987, 1989). LSRs calculated for the Late Cretaceous through Paleogene clay section at DSDP Site 576 averaged about 0.4–0.5 m/m.y. (Heath, Burckle, et al., 1985; Janecek, 1985). If we assume that the red clays at Sites 885/886 accumulated continuously and with similar average LSRs as at Site 576, then the 20-m-thick sequence recovered at these sites represents 30–40 m.y. of deposition, and the underlying basalts are Eocene or older in age.

Since late Miocene time, pelagic clays and biogenic silica have accumulated in the region. Diatoms appear in sediments of Sites 885 and 886 at approximately 9.5 Ma and greatly increase in abundance at about 7.5 Ma, distinctly marking the boundary between pre-upper Miocene brown clays and upper Miocene–upper Pliocene yellowish-brown clayey diatom ooze. Sedimentation rates increase to average values of 5.7 m/m.y. This well-defined interval of increased diatom flux (to about 190 $mg(cm^2 \cdot k.y.)^{-1}$ coincides with a period of enhanced biogenic silica supply in the North Pacific Ocean that was observed in all other Leg 145 Sites. However, owing to the location of Sites 885/886 under low productivity oligotrophic waters, MARs of silica are lower here than at the more northerly drill sites. Diatom supply decreased during the late Pliocene to an average of 20 $mg(cm^2 \cdot k.y.)^{-1}$.

Upper Miocene–Quaternary clays at Sites 885/886 differ from older clays at these sites; they are more similar to clays that compose the upper part of abyssal pelagic sequences throughout the central North Pacific Ocean (McManus, Burns, et al., 1970; Thiede, Vallier, et al., 1981; Heath, Burckle, et al., 1985). Unlike the older brown clays, the younger clays generally contain more quartz and other eolian terrigenous material (Leinen, 1989).

Clay fluxes at Sites 885 and 886 in the late Miocene through late Pliocene remain low, averaging about 30 $mg(cm^2 \cdot k.y.)^{-1}$, but increase to approximately 180 $mg(cm^2 \cdot k.y.)^{-1}$ near the Matuyama/Gauss boundary (approximately 2.6 Ma). These MARs are comparable to those obtained for eolian material from late Cenozoic sequences elsewhere in the central North Pacific Ocean (Rea and Janecek, 1982; Janecek, 1985; Rea et al., 1985), with the large increase in Pliocene MARs resulting from increased eolian influx from Asia at the onset of major Northern Hemisphere glaciation.

The occurrence of ferro-manganese nodules in red clays in the lower part of the sequence at Sites 885/886 is consistent with low sedimentation rates and low organic carbon content (<0.1%) determined for these sediments. At the same time, occurrence of centimeter-scale ferro-manganese nodules in Miocene diatom ooze suggests that the influx of chemical elements from hydrothermal sources also occurred at that time. Determination of the nature of these nodules awaits more detailed, shore-based study; however, several factors suggest that diagenetic processes did not contribute much to their formation. These factors include (1) the rounded or botryoidal shape of the nodules, (2) the low organic carbon concentration, and (3) the presence of other oxidized forms of iron in the sediments. The relatively large dimensions of the nodules also favor a hydrothermal source for their formation. At the seafloor, under the influence of a hydrogenous source, nodules form very slowly, growing at rates averaging 2 mm/m.y. (Bogdanov et al., 1990). Formation of the large nodules that can be observed in the upper Miocene–Pliocene sediments of Sites 885/886 would have required at least 30 m.y.

REFERENCES*

Barron, J.A., and Baldauf, J.G., 1990. Development of biosiliceous sedimentation in the North Pacific during the Miocene and Early Pliocene. *In* Tsuchi, R. (Ed.), *Pacific Neogene Events: Their Timing, Nature and Interrelationship:* Tokyo (Univ. of Tokyo Press), 43–63.

Bogdanov, Y.A., Sorokhtin, O.G., and Zonenshain, L.P., 1990. *Ferro-manganese Crusts and Nodules from the Pacific Undersea Mounts:* Moscow (Nauka). (in Russian)

Bryant, W.R., Wetzel, A., Taylor, E., and Sweet, W.E., 1986. Consolidation characteristics and permeability of Mississippi Fan sediments. *In* Bouma, A.H., Coleman, J.M., Meyer, A.W., et al., *Init. Repts. DSDP,* 96: Washington (U.S. Govt. Printing Office), 797–809.

Cande, S.C., and Kent, D.V., 1992. A new geomagnetic polarity timescale for the Late Cretaceous and Cenozoic. *J. Geophys. Res.,* 97:13917–13951.

Chester, R., 1990. *Marine Geochemistry*: London (Unwin Hyman).

Creager, J.S., Scholl, D.W., et al., 1973. *Init. Repts. DSDP,* 19: Washington (U.S. Govt. Printing Office).

Cronan, D.S., 1980. *Underwater Minerals*: London (Academic Press).

Deer, W.A., Howie, R.A., and Zussman, J., 1966. *An Introduction to the Rock-Forming Minerals:* London (Longman Group).

Foreman, H.P., 1975. Radiolaria from the North Pacific, Deep Sea Drilling Project, Leg 32. *In* Larson, R.L., Moberly, R., et al., *Init. Repts. DSDP,* 32: Washington (U.S. Govt. Printing Office), 579–676.

Hays, J.D., 1970. Stratigraphy and evolutionary trends of radiolaria in North Pacific deep sea sediments. *In* Hays, J.D. (Ed.), *Geological Investigations of the North Pacific.* Mem.—Geol. Soc. Am., 126:185–218.

Heath, G.R., Burckle, L.H., et al., 1985. *Init. Repts. DSDP,* 86: Washington (U.S. Govt. Printing Office), 459–502.

Heath, G.R., Rea, D.H., and Levi, S., 1985. Paleomagnetism and accumulation rates of sediments at Sites 576 and 578, Deep Sea Drilling Project Leg 86, western North Pacific Ocean. *In* Heath, G.R., Burckle, L.H., et al., *Init. Repts. DSDP,* 86: Washington (U.S. Govt. Printing Office).

Janecek, T.R., 1985. Eolian sedimentation in the Northwest Pacific Ocean: a preliminary examination of the data from Deep Sea Drilling Project Sites 576 and 578. *In* Heath, G.R., Burckle, L.H., et al., *Init. Repts. DSDP,* 86: Washington (U.S. Govt. Printing Office), 589–603.

Janecek, T.R., and Rea, D.K., 1983. Eolian deposition in the northeast Pacific Ocean: Cenozoic history of atmospheric circulation. *Geol. Soc. Am. Bull.,* 94:730–738.

Kadko, D., 1985. Late Cenozoic sedimentation and metal deposition in the North Pacific. *Geochim. Cosmochim. Acta,* 49:651–661.

Koizumi, I., and Tanimura, Y., 1985. Neogene diatom biostratigraphy of the middle latitude western North Pacific, Deep Sea Drilling Project Leg 86. *In* Heath, G.R., Burckle, L.H., et al., *Init. Repts. DSDP,* 86: Washington (U.S. Govt. Printing Office), 269–300.

Kyte, F.T., and Wasson, J.T., 1986. Accretion rate of extraterrestrial matter: iridium deposited 33 to 67 million years ago. *Science,* 232:1225–1229.

Landing, W.M., and Bruland, K.W., 1980. Manganese in the North Pacific. *Earth Planet. Sci. Lett.,* 49:45–46.

Leinen, M., 1987. The origin of paleochemical signatures in North Pacific pelagic clays: partitioning experiments. *Geochim. Cosmochim. Acta,* 51:305–319.

———, 1989. The pelagic clay province of the North Pacific Ocean. *In* Winterer, E.L., Hussong, D.M., and Decker, R.W. (Eds.), *The Geology of North America* (Vol. N): *The Eastern Pacific Ocean and Hawaii.* Geol. Soc. Am., 323–335.

Leinen, M., and Heath, G.R., 1981. Sedimentary indicators of atmospheric circulation in the Northern Hemisphere during the Cenozoic. *Palaeogeogr., Palaeoclimatol., Palaeoecol.,* 36:1–21.

Lyle, M., Owen, R., and Leinen, M., 1986. History of hydrothermal sedimentation at the east Pacific Rise, 19°S. *In* Leinen, M., Rea, D.K., et al., *Init. Repts. DSDP*, 92: Washington (U.S. Govt. Printing Office).

* Abbreviations for names of organizations and publication titles in ODP reference lists follow the style given in *Chemical Abstracts Service Source Index* (published by American Chemical Society).

McCoy, F.W., and Sancetta, C., 1985. North Pacific Ocean sediments. *In* Nairn, A.E.M., Stehli, F.G., and Uyeda, S. (Eds.), *The Ocean Basins and Margins* (Vol. 7): *The Pacific Ocean*: New York (Plenum), 1–64.

McDuff, R.E., 1985. The chemistry of interstitial waters, Deep Sea Drilling Project, Leg 86. *In* Heath, G.R., Burckle, L.H., et al., *Init. Repts. DSDP,* 86: Washington (U.S. Govt. Printing Office), 675–687.

McManus, D.A., Burns, R.E., et al., 1970. *Init. Repts. DSDP,* 5: Washington (U.S. Govt. Printing Office).

Owen, R.M., and Rea, D.K., 1985. Sea-floor hydrothermal activity links climate to tectonics: the Eocene CO2 greenhouse. *Science,* 227:166–169.

Rea, D.K., and Dixon, J.M., 1983. Late Cretaceous and Paleogene tectonic evolution of the North Pacific Ocean. *Earth Planet. Sci. Lett.,* 65:145–166.

Rea, D.K., and Janecek, T.R., 1982. Late Cenozoic changes in atmospheric circulation deduced from North Pacific eolian sediments. *Mar. Geol.,* 49:149–167.

Rea, D.K., Leinen, M., and Janecek, T.R., 1985. Geologic approach to the long-term history of atmospheric circulation. *Science,* 227:721–725.

Skempton, A.W., 1970. The consolidation of clays by gravitational compaction. *Q. J. Geol. Soc. London,* 125:373–411.

Thiede, J., Vallier, T.L., et al., 1981. *Init. Repts. DSDP*, 62: Washington (U.S. Govt. Printing Office).

Ms 145IR-109

NOTE: For all sites drilled, core-description forms ("barrel sheets") and core photographs can be found in Section 3, beginning on page 395. Forms containing smear-slide data can be found in Section 4, beginning on page 985. Thin-section data are given in Section 5, beginning on page 1013.

Table 6. Listing of average sediment data and flux results for two time-stratigraphic intervals at Sites 885/886.

Depth int. (mbsf)	Age int. (Ma)	Dry-bulk density (g/cm^3)	Linear sed. rate (cm/k.y.)	Diatom		Clay		Glass		Quartz		Carbonate		TOC	
				(%)	($g[cm^2 \cdot k.y.]^{-1}$)	(%)	($g[cm^2 \cdot k.y.]^{-1}$)	(%)	($g[cm^2 \cdot k.y.]^{-1}$)	(%)	($g[cm^2 \cdot k.y.]^{-1}$)	(%)	($g[cm^2 \cdot k.y.]^{-1}$)	(%)	($g[cm^2 \cdot k.y.]^{-1}$)
0–17	0.0–3.0	0.45	0.57	8.1	0.021	69.6	0.178	0.75	0	2.9	0.07	0	0	0.07	0
17–52	3.0–9.4	0.41	0.57	81.4	0.19	13.6	0.032	0	0	0	0	0	0	0.08	0

Table 6 (continued).

Table 7. Interstitial-water data for Site 886.

Core, section, interval (cm)	Depth (mbsf)	pH	Alk. (mM)	S (g/kg)	Cl (mM)	Mg (mM)	Ca (mM)	SO_4 (mM)	NH_4 (µM)	NO_2 (µM)	H_4SiO_4 (µM)	K (mM)	Li (µM)	Na (mM)	Sr (µM)	Mn (µM)	Mg/Ca (mol ratio)
145-886A-																	
1H-1, 145-150	3.45	7.33	2.72	34.5	555	52.50	10.46	28.2	0	0	551	11.31	28.3	477	93.7	2.1	5.02
1H-2, 145-150	4.95	7.57	2.67	34.3	555	52.28	10.44	28.0	0	0	575	11.53	29.9	477	93.4	2.1	5.01
1H-3, 145-150	6.45	7.59	2.49	34.3	554	52.04	10.43	27.8	0	0	615	11.09	30.4	476	95.6	2.8	4.99
1H-4, 145-150	7.95	7.56	2.53	34.3	554	52.61	10.34	27.8	0	0	595	11.15	28.9	475	92.3	1.9	5.09
145-886B-																	
1H-1, 115-120	1.65	7.60	2.63	35.0	554	51.67	10.32	27.6	0	0	583	10.86	31.5	477	92.4	4.9	5.01
2H-4, 145-150	7.75	7.60	2.60	35.0	557	52.28	10.44	27.8	0	0	612	11.09	29.2	478	90.8	12.4	5.01
3H-4, 145-150	17.25	7.63	2.74	35.0	563	52.80	10.72	28.4	0	0	717	10.77	29.4	485	91.6	25.1	4.92
4H-4, 145-150	26.75	7.51	2.69	35.3	564	53.84	10.90	28.6	93	n.m.	764	9.97	29.7	484	97.1	28.4	4.94
5H-4, 145-150	36.25	7.63	2.62	35.5	563	54.04	10.87	28.8	154	n.m.	800	10.29	30.7	483	95.2	23.1	4.97
6H-4, 145-150	45.75	7.57	2.58	36.0	561	53.94	10.88	28.6	19	n.m.	717	10.16	30.5	481	98.5	21.0	4.96
7H-4, 145-150	55.75	7.55	2.52	35.5	560	51.99	10.57	27.1	70	n.m.	698	10.29	31.6	481	87.5	16.0	4.92

Table 8. Results of headspace gas analyses from Hole 885A.

Core, section, interval (cm)	Depth (mbsf)	C_1 (ppm)
145-885A-		
1H-2, 0–3	1.5	2
2H-5, 0–3	10.6	4
3H-5, 0–3	20.1	3
4H-5, 0–3	29.6	4
5H-5, 0–3	39.1	5
6H-5, 0–3	48.6	2

Note: C_1 = methane. All samples are headspace samples.

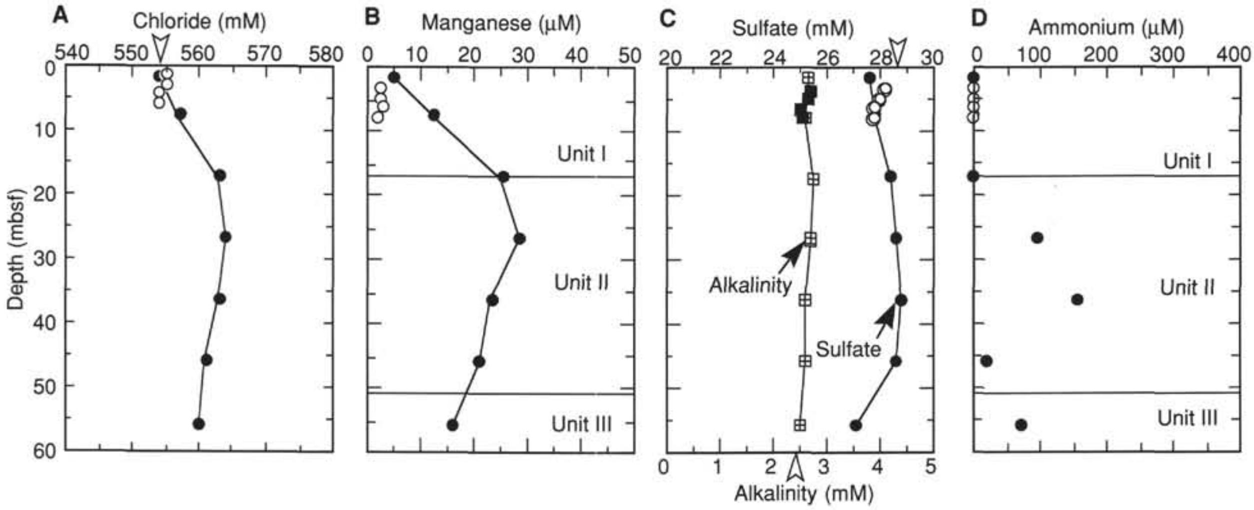

Figure 13. Interstitial-water profiles for Site 886. **A.** Chloride for Holes 886A and 886B. **B.** Manganese composite profile for Holes 886A and 886B. Horizontal lines at 17.3 and 50.3 mbsf represent lithologic boundaries among Units I, II, and III at Hole 886B. **C.** Sulfate and alkalinity composite profile for Holes 886A and 886B. **D.** Ammonium composite profile for Holes 886A and 886B. Open and closed circles indicate data from Holes 886A and 886B, respectively. The open arrowhead indicates the chloride concentration in modern North Pacific Deep Water.

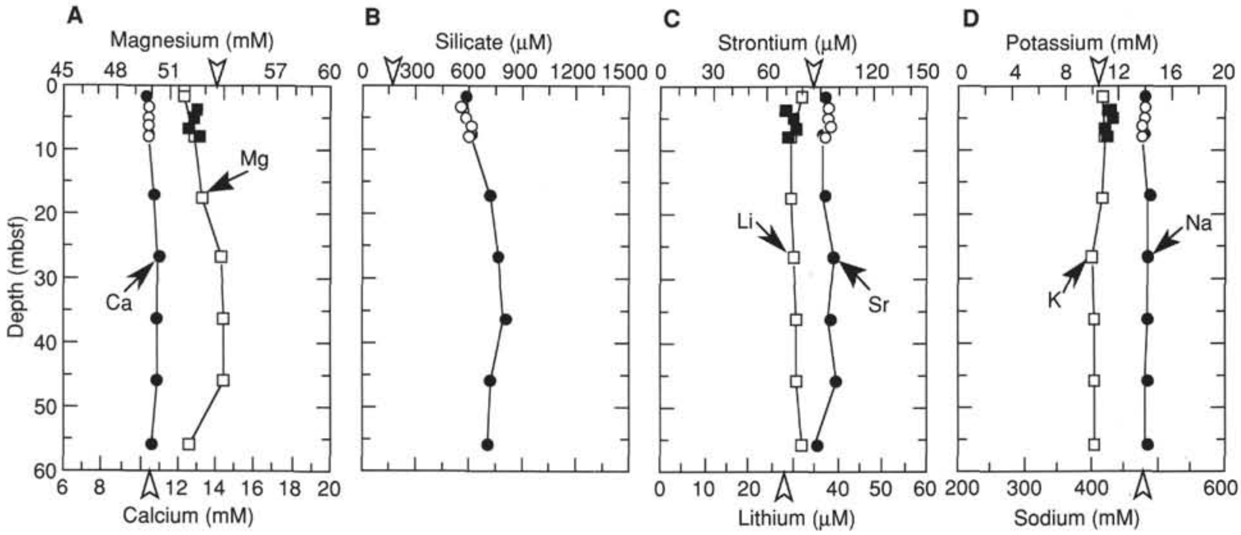

Figure 14. **A.** Magnesium and calcium composite profiles for Holes 886A and 886B. **B.** Silicate composite profile for Holes 886A and 886B. Horizontal lines at 17.3 and 50.3 mbsf represent lithologic boundaries among Units I, II, and III at Hole 886B. **C.** Strontium and lithium composite profiles for Holes 884A and 886B. **D.** Potassium and sodium composite profiles for Holes 886A and 886B. Open circles and closed squares represent data from Hole 886A, while closed circles and open squares mark data from Hole 886B. The open arrowhead indicates the concentration in modern North Pacific Deep Water.

Table 9. Results of headspace gas analyses from Holes 886A, 886B, and 886C.

Core, section, interval (cm)	Depth (mbsf)	C_1 (ppm)
145-886A-		
1H-5, 0–3	6.0	3
145-886B-		
2H-5, 0–3	7.8	2
3H-5, 0–3	17.3	2
4H-5, 0–3	26.8	2
5H-5, 0–3	36.3	2
6H-5, 0–3	45.8	2
7H-5, 0–3	55.3	2
145-886C-		
1H-3, 0–3	3.0	2
2H-4, 0–3	11.3	2
3H-5, 0–3	22.3	2
4H-4, 0–3	30.3	2
5H-2, 0–3	36.8	2
6H-5, 0–3	50.8	2
7H-5, 0–3	60.3	2

Note: C_1 = methane. All samples are headspace samples.

Table 10. Results of geochemical analyses from Hole 885A.

Core, section, interval (cm)	Depth (mbsf)	TC (wt%)	IC (wt%)	TOC (wt%)	$CaCO_3$ (wt%)	TN (wt%)
145-885A-						
1H-1, 76–77	0.76	0.13	0	0.13	0	0.07
1H-2, 71–72	2.21	0.07	0	0.07	0	0.00
1H-3, 91–92	3.91	0.09	0	0.09	0	0.00
2H-1, 76–77	5.36	0.06	0	0.06	0	0.00
2H-2, 76–77	6.86	0.10	0	0.10	0	0.00
2H-3, 76–77	8.36	0.06	0	0.06	0	0.00
2H-4, 76–77	9.86	0.06	0	0.06	0	0.00
2H-5, 76–77	11.36	0.06	0	0.06	0	0.00
2H-6, 76–77	12.86	0.06	0	0.06	0	0.00
3H-1, 72–73	14.82	0.08	0	0.08	0	0.00
3H-2, 72–73	16.32	0.04	0	0.04	0	0.00
3H-3, 73–74	17.83	0.07	0	0.07	0	0.00
3H-4, 72–73	19.32	0.08	0	0.08	0	0.00
3H-5, 72–73	20.82	0.10	0	0.10	0	0.00
3H-6, 72–73	22.32	0.12	0	0.12	0	0.04
3H-7, 72–73	23.82	0.14	0	0.14	0	0.05
4H-1, 81–82	24.41	0.10	0	0.10	0	0.00
4H-2, 76–77	25.86	0.08	0	0.08	0	0.00
4H-3, 76–77	27.36	0.09	0	0.09	0	0.00
4H-4, 76–77	28.86	0.09	0	0.09	0	0.03
4H-5, 76–77	30.36	0.08	0	0.08	0	0.04
4H-6, 76–77	31.86	0.08	0	0.08	0	0.00
4H-7, 76–77	33.36	0.08	0	0.08	0	0.04
5H-1, 73–74	33.83	0.10	0	0.10	0	0.04
5H-2, 73–74	35.33	0.06	0	0.06	0	0.00
5H-3, 73–74	36.83	0.06	0	0.06	0	0.04
5H-4, 73–74	38.33	0.07	0	0.07	0	0.05
5H-5, 73–74	39.83	0.08	0	0.08	0	0.04
5H-6, 73–74	41.33	0.08	0	0.08	0	0.04
5H-7, 37–38	42.47	0.07	0	0.07	0	0.04
6H-1, 77–78	43.37	0.05	0	0.05	0	0.03
6H-2, 72–73	44.82	0.07	0	0.07	0	0.05
6H-3, 72–73	46.32	0.08	0	0.08	0	0.05
6H-4, 72–73	47.82	0.06	0	0.06	0	0.03
6H-5, 77–78	49.37	0.07	0	0.07	0	0.00
6H-6, 72–73	50.82	0.04	0	0.04	0	0.02
6H-7, 17–18	51.65	0.03	0	0.03	0	0.00

Note: TC = total carbon, IC = inorganic carbon, and TN = total nitrogen. All results are given in weight percent of bulk dry sediment.

Table 11. Results of geochemical analyses from Hole 886B.

Core, section, interval (cm)	Depth (mbsf)	TC (wt%)	IC (wt%)	TOC (wt%)	$CaCO_3$ (wt%)	TN (wt%)
145-886B-						
2H-1, 72–73	2.52	0.22	0	0.22	0	0.00
2H-2, 72–73	4.02	0.08	0	0.08	0	0.02
2H-3, 72–73	5.52	0.08	0	0.08	0	0.04
2H-4, 72–73	7.02	0.09	0	0.09	0	0.04
2H-5, 72–73	8.52	0.13	0	0.13	0	0.05
2H-6, 72–73	10.02	0.12	0	0.12	0	0.04
2H-7, 51–52	11.31	0.14	0	0.14	0	0.04
3H-1, 71–72	12.01	0.08	0	0.08	0	0.04
3H-2, 66–67	13.46	0.07	0	0.07	0	0.03
3H-3, 72–73	15.02	0.08	0	0.08	0	0.05
3H-4, 71–72	16.51	0.09	0	0.09	0	0.04
3H-5, 67–68	17.97	0.08	0	0.08	0	0.03
3H-6, 72–73	19.52	0.09	0	0.09	0	0.02
4H-1, 72–73	21.52	0.10	0	0.10	0	0.03
4H-2, 72–73	23.02	0.08	0	0.08	0	0.03
4H-3, 72–73	24.52	0.11	0	0.11	0	0.02
4H-4, 72–73	26.02	0.17	0	0.17	0	0.02
4H-5, 72–73	27.52	0.25	0	0.25	0	0.03
4H-6, 72–73	29.02	0.20	0	0.20	0	0.03
5H-1, 72–73	31.02	0.18	0	0.18	0	0.00
5H-2, 72–73	32.52	0.09	0	0.09	0	0.02
5H-3, 72–73	34.02	0.13	0	0.13	0	0.03
5H-4, 72–73	35.52	0.12	0	0.12	0	0.03
5H-5, 72–73	37.02	0.10	0	0.10	0	0.00
5H-6, 72–73	38.52	0.15	0	0.15	0	0.02
5H-7, 72–73	40.02	0.11	0	0.11	0	0.04
6H-1, 72–73	40.52	0.08	0	0.08	0	0.00
6H-2, 72–73	42.02	0.04	0	0.04	0	0.04
6H-3, 72–73	43.52	0.13	0	0.13	0	0.05
6H-4, 72–73	45.02	0.09	0	0.09	0	0.00
6H-5, 72–73	46.52	0.08	0	0.08	0	0.04
6H-6, 72–73	48.02	0.10	0	0.10	0	0.07
7H-1, 72–73	50.02	0.07	0	0.07	0	0.04
7H-2, 72–73	51.52	0.10	0	0.10	0	0.06
7H-3, 72–73	53.02	0.08	0	0.08	0	0.06
7H-4, 72–73	54.52	0.07	0	0.07	0	0.00
7H-5, 72–73	56.02	0.03	0	0.03	0	0.04
7H-6, 71–72	57.51	0.02	0	0.02	0	0.00
7H-7, 41–42	58.71	0.05	0	0.05	0	0.00

Note: TC = total carbon, IC = inorganic carbon, and TN = total nitrogen. All results given in weight percent of bulk dry sediment.

Table 12. Summary of physical properties measurements at Site 885/886.

	Hole 885A	Hole 886A	Hole 886B	Hole 886C
Shear strength				
Motorized vane	x	x	x	x
Compressional wave velocity				
P-wave logger	x	x	x	x
Digital sediment velocimeter	x	x	x	x
Index properties				
Shipboard analysis	x	x	x	x
Thermal conductivity				
Needle probe	x	-	x	x

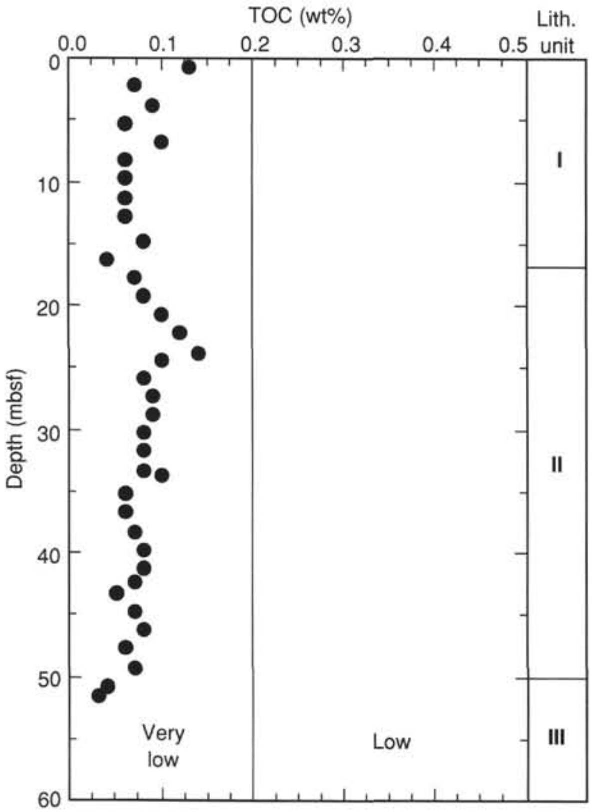

Figure 15. Total organic carbon contents vs. depth, Hole 885A. Lithologic units are shown at right.

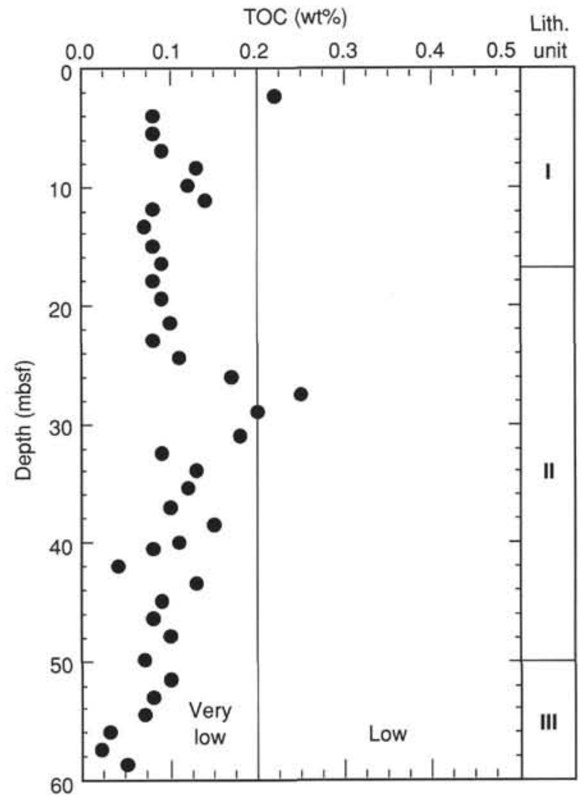

Figure 16. Total organic carbon contents vs. depth, Hole 886B. Lithologic units are shown at right.

Table 13. Index properties data from Hole 885A.

Core, section, interval (cm)	Depth (mbsf)	Wet-bulk density (g/cm³)	Dry-bulk density (g/cm³)	Grain density (g/cm³)	Wet porosity (%)	Dry porosity (%)	Wet water content (%)	Dry water content (%)	Void ratio 1	Void ratio 2
145-885A-										
1H-1, 74	0.74	1.30	0.47	2.60	81.80	82.40	64.00	178.10	4.50	4.59
1H-2, 69	2.19	1.30	0.44	2.72	83.30	83.90	65.80	192.10	4.98	5.09
1H-3, 89	3.89	1.32	0.50	2.58	80.10	80.70	62.00	163.10	4.03	4.11
2H-1, 74	5.34	1.32	0.51	2.49	79.10	79.70	61.30	158.60	3.79	3.86
2H-2, 74	6.84	1.29	0.46	2.47	81.10	81.70	64.50	181.40	4.30	4.38
2H-3, 74	8.34	1.33	0.53	2.49	78.40	79.00	60.30	151.60	3.62	3.68
2H-4, 74	9.84	1.27	0.41	2.56	83.60	84.20	67.60	208.80	5.10	5.22
2H-5, 74	11.34	1.29	0.45	2.47	81.30	81.90	64.80	184.30	4.35	4.44
2H-6, 74	12.84	1.22	0.37	2.28	83.50	84.20	70.00	233.50	5.07	5.19
3H-1, 74	14.84	1.22	0.36	2.22	83.30	84.00	70.20	235.40	4.99	5.11
3H-2, 74	16.34	1.27	0.43	2.38	81.40	82.10	65.90	193.00	4.39	4.48
3H-3, 74	17.84	1.19	0.33	2.09	84.00	84.80	72.60	264.70	5.26	5.39
3H-4, 74	19.34	1.19	0.32	2.14	84.50	85.30	72.80	268.10	5.47	5.61
3H-5, 74	20.84	1.17	0.29	2.06	85.40	86.20	75.00	299.70	5.86	6.02
3H-6, 74	22.34	1.18	0.30	2.25	86.20	86.90	74.50	292.70	6.25	6.43
3H-7, 73	23.84	1.24	0.40	2.23	81.50	82.20	67.40	206.40	4.41	4.50
4H-1, 79	24.39	1.17	0.29	2.05	85.20	86.00	74.80	296.70	5.77	5.93
4H-2, 74	25.84	1.19	0.32	2.23	85.20	86.00	73.10	272.40	5.78	5.93
4H-3, 74	27.34	1.24	0.40	2.31	82.40	83.00	67.90	211.50	4.67	4.77
4H-4, 74	28.84	1.23	0.38	2.19	82.10	82.80	68.60	218.40	4.58	4.67
4H-5, 74	30.34	1.26	0.44	2.27	80.20	80.90	65.10	186.90	4.06	4.13
4H-6, 74	31.84	1.22	0.38	2.18	82.10	82.80	68.80	220.70	4.60	4.70
4H-7, 74	33.34	1.34	0.58	2.31	74.60	75.20	56.90	132.20	2.94	2.98
5H-1, 74	33.84	1.27	0.45	2.35	80.50	81.10	64.70	183.60	4.13	4.20
5H-2, 74	35.34	1.21	0.36	2.17	83.00	83.80	70.30	236.80	4.90	5.01
5H-3, 74	36.84	1.24	0.39	2.28	82.50	83.20	68.40	216.80	4.72	4.82
5H-4, 74	38.34	1.20	0.34	2.16	84.00	84.70	71.80	255.00	5.25	5.38
5H-5, 74	39.84	1.30	0.49	2.40	79.20	79.80	62.30	165.30	3.80	3.86
5H-6, 74	41.34	1.30	0.47	2.49	80.90	81.50	64.00	177.50	4.24	4.32
5H-7, 39	42.49	1.27	0.43	2.52	82.70	83.30	66.50	198.60	4.78	4.89
6H-1, 79	43.39	1.23	0.38	2.34	83.30	84.00	69.10	224.10	5.00	5.12
6H-2, 74	44.84	1.30	0.44	2.71	83.20	83.80	65.80	192.20	4.97	5.08
6H-3, 74	46.34	1.31	0.46	2.71	82.60	83.20	64.70	183.10	4.73	4.84
6H-4, 74	47.84	1.41	0.62	2.70	76.50	77.10	55.70	125.80	3.26	3.31
6H-5, 79	49.39	1.29	0.44	2.59	82.60	83.20	65.70	191.80	4.75	4.85
6H-6, 74	50.84	1.34	0.46	3.39	86.00	86.60	65.70	191.40	6.15	6.33
6H-7, 19	51.67	1.31	0.42	3.25	86.70	87.30	68.00	212.20	6.53	6.73

Table 14. Index properties data from Hole 886A.

Core, section, interval (cm)	Depth (mbsf)	Wet-bulk density (g/cm^3)	Dry-bulk density (g/cm^3)	Grain density (g/cm^3)	Wet porosity (%)	Dry porosity (%)	Wet water content (%)	Dry water content (%)	Void ratio 1	Void ratio 2
145-886A-										
1H-1, 0	1.29	1.33	0.52	2.58	79.50	80.10	61.00	156.60	3.88	3.94
1H-2, 129	2.79	1.33	0.51	2.62	80.10	80.70	61.60	160.10	4.01	4.09
1H-3, 129	4.29	1.36	0.54	2.77	80.00	80.60	60.10	150.70	4.01	4.08
1H-4, 129	5.79	1.32	0.47	2.74	82.40	83.00	64.10	178.40	4.67	4.78
1H-5, 136	7.36	1.33	0.50	2.66	80.90	81.50	62.40	166.20	4.23	4.31
1H-6, 136	8.86	1.27	0.41	2.62	83.90	84.50	67.60	208.90	5.21	5.34
1H-7, 29	9.29	1.33	0.51	2.63	80.10	80.70	61.50	159.80	4.03	4.10

Table 15. Index properties data from Hole 886B.

Core, section, interval (cm)	Depth (mbsf)	Wet-bulk density (g/cm^3)	Dry-bulk density (g/cm^3)	Grain density (g/cm^3)	Wet porosity (%)	Dry porosity (%)	Wet water content (%)	Dry water content (%)	Void ratio 1	Void ratio 2
145-886B-										
1H-1, 69	0.69	1.32	0.48	2.73	82.20	82.80	63.90	177.10	4.62	4.72
1H-2, 15	1.35	1.32	0.50	2.59	80.50	81.10	62.50	166.40	4.12	4.20
2H-1, 69	2.49	1.35	0.54	2.58	78.50	79.10	59.70	147.90	3.66	3.72
2H-2, 69	3.99	1.28	0.44	2.46	81.60	82.20	65.30	188.30	4.43	4.52
2H-3, 69	5.49	1.32	0.48	2.64	81.40	82.00	63.40	173.00	4.37	4.46
2H-5, 69	8.49	1.34	0.53	2.64	79.70	80.30	60.80	155.00	3.93	4.00
2H-6, 69	9.99	1.38	0.57	2.70	78.40	78.90	58.30	139.70	3.62	3.68
2H-7, 49	11.29	1.34	0.52	2.67	80.20	80.80	61.30	158.50	4.05	4.13
3H-1, 69	11.99	1.33	0.51	2.60	80.00	80.60	61.60	160.30	4.00	4.07
3H-2, 64	13.44	1.27	0.43	2.52	82.60	83.30	66.40	197.70	4.75	4.86
3H-3, 69	14.99	1.32	0.50	2.56	80.10	80.70	62.10	164.10	4.03	4.11
3H-4, 69	16.49	1.28	0.44	2.46	81.60	82.30	65.30	188.40	4.44	4.53
3H-5, 69	17.99	1.24	0.40	2.24	81.80	82.40	67.60	208.70	4.48	4.57
3H-6, 69	19.49	1.27	0.43	2.38	81.50	82.10	65.90	193.60	4.40	4.49
4H-1, 69	21.49	1.27	0.42	2.43	82.20	82.90	66.60	199.30	4.63	4.73
4H-2, 69	22.99	1.24	0.41	2.24	81.20	81.80	66.80	201.20	4.31	4.39
4H-3, 69	24.49	1.19	0.32	2.17	84.70	85.40	72.80	267.40	5.52	5.66
4H-4, 69	25.99	1.19	0.33	2.17	84.50	85.20	72.50	264.10	5.44	5.58
4H-5, 69	27.49	1.18	0.31	2.20	85.70	86.40	74.10	286.70	5.99	6.16
4H-6, 69	28.99	1.20	0.32	2.25	85.40	86.10	73.10	272.00	5.83	5.99
5H-1, 69	30.99	1.14	0.25	2.03	87.20	88.00	78.00	355.20	6.81	7.02
5H-2, 69	32.49	1.19	0.31	2.23	85.90	86.60	74.20	288.20	6.09	6.26
5H-3, 69	33.99	1.25	0.43	2.21	80.10	80.80	65.50	189.90	4.02	4.09
5H-4, 69	35.49	1.27	0.45	2.32	80.30	80.90	64.70	183.00	4.07	4.14
5H-5, 69	36.99	1.22	0.37	2.27	83.20	83.90	69.70	229.60	4.96	5.08
5H-6, 69	38.49	1.23	0.37	2.30	83.50	84.20	69.80	231.50	5.07	5.19
5H-7, 69	39.99	1.29	0.48	2.39	79.60	80.20	63.00	170.60	3.91	3.98
6H-1, 69	40.49	1.24	0.39	2.29	82.70	83.30	68.60	218.00	4.76	4.87
6H-2, 69	41.99	1.26	0.43	2.25	80.40	81.10	65.60	190.80	4.11	4.19
6H-3, 69	43.49	1.24	0.39	2.37	83.30	84.00	68.80	220.70	4.98	5.10
6H-4, 69	44.99	1.19	0.34	2.12	83.70	84.50	71.80	255.00	5.15	5.27
6H-5, 69	46.49	1.27	0.45	2.36	80.70	81.40	64.90	185.20	4.19	4.27
6H-6, 69	47.99	1.30	0.47	2.48	80.70	81.40	63.80	176.50	4.19	4.27
7H-1, 69	49.99	1.29	0.44	2.68	83.30	83.90	66.00	194.30	4.97	5.09
7H-2, 69	51.49	1.32	0.47	2.85	82.90	83.50	64.20	179.10	4.86	4.97
7H-3, 69	52.99	1.45	0.68	2.75	75.00	75.60	53.10	113.40	3.00	3.04
7H-4, 69	54.49	1.38	0.57	2.76	78.80	79.40	58.40	140.50	3.72	3.79
7H-5, 69	55.99	1.39	0.59	2.70	77.80	78.30	57.40	135.00	3.50	3.55
7H-6, 69	57.49	1.33	0.50	2.68	80.80	81.40	62.20	164.20	4.21	4.29
7H-7, 39	58.69	1.37	0.58	2.55	76.70	77.30	57.40	134.50	3.30	3.35
8X-1, 39	59.19	1.37	0.50	3.38	84.90	85.50	63.60	174.90	5.62	5.77

Table 16. Index properties data from Hole 886C.

Core, section, interval (cm)	Depth (mbsf)	Wet-bulk density (g/cm^3)	Dry-bulk density (g/cm^3)	Grain density (g/cm^3)	Wet porosity (%)	Dry porosity (%)	Wet water content (%)	Dry water content (%)	Void ratio 1	Void ratio 2
145-886C-										
1H-1, 68	0.68	1.32	0.48	2.70	81.80	82.40	63.60	175.10	4.49	4.59
1H-2, 69	2.19	1.32	0.49	2.68	81.30	81.90	62.90	169.80	4.36	4.44
1H-3, 68	3.68	1.28	0.43	2.56	82.80	83.50	66.40	197.30	4.83	4.93
1H-4, 68	5.18	1.26	0.41	2.51	83.30	83.90	67.60	208.20	4.98	5.10
1H-5, 50	6.50	1.37	0.56	2.75	79.30	79.80	59.20	144.90	3.82	3.89
2H-1, 69	7.49	1.34	0.53	2.59	79.10	79.70	60.40	152.40	3.79	3.85
2H-2, 69	8.99	1.29	0.44	2.67	83.30	84.00	66.20	196.30	5.01	5.12
2H-3, 69	10.49	1.34	0.52	2.67	80.10	80.70	61.10	157.40	4.03	4.10
2H-4, 69	11.99	1.37	0.55	2.80	79.90	80.50	59.70	148.40	3.98	4.05
2H-4, 137	12.67	1.31	0.48	2.58	81.00	81.60	63.30	172.30	4.26	4.34
2H-5, 69	13.49	1.31	0.46	2.69	82.40	83.00	64.50	181.80	4.67	4.77
3H-6, 56	24.36	1.23	0.41	2.14	80.70	81.40	67.10	204.10	4.19	4.27
3H-1, 79	17.09	1.31	0.48	2.58	80.80	81.40	63.10	171.00	4.22	4.30
3H-2, 69	18.49	1.22	0.37	2.27	83.20	83.90	69.60	228.80	4.95	5.06
3H-3, 68	19.98	1.27	0.43	2.41	81.60	82.30	65.90	192.90	4.44	4.53
3H-4, 71	21.51	1.26	0.42	2.39	82.20	82.80	66.90	202.10	4.61	4.71
3H-5, 68	22.98	1.27	0.44	2.35	80.90	81.50	65.20	187.50	4.23	4.31
3H-5, 135	23.65	1.23	0.38	2.22	82.50	83.10	68.90	221.80	4.70	4.80
4H-6, 69	33.99	1.25	0.41	2.33	82.10	82.80	67.30	206.20	4.60	4.70
4H-7, 49	34.79	1.24	0.40	2.24	81.80	82.50	67.70	210.10	4.51	4.60
4H-1, 69	26.49	1.18	0.31	2.06	84.60	85.30	73.60	279.00	5.47	5.61
4H-2, 69	27.99	1.17	0.28	2.16	86.40	87.20	75.70	311.10	6.38	6.57
4H-3, 69	29.49	1.22	0.36	2.23	83.40	84.10	70.30	236.20	5.03	5.15
4H-4, 69	30.99	1.16	0.27	2.14	87.10	87.80	76.90	332.00	6.74	6.95
4H-4, 134	31.64	1.17	0.28	2.20	86.70	87.40	75.80	313.20	6.51	6.71
4H-5, 69	32.49	1.15	0.27	2.01	86.00	86.80	76.30	321.90	6.13	6.31
4H-6, 69	33.99	1.18	0.30	2.20	85.70	86.50	74.30	288.60	6.02	6.18
4H-7, 39	34.69	1.24	0.40	2.33	82.50	83.20	68.00	212.30	4.72	4.82
5H-1, 69	35.99	1.23	0.39	2.26	82.60	83.30	68.70	219.40	4.74	4.85
5H-2, 69	37.49	1.22	0.35	2.29	84.20	84.90	71.00	244.70	5.34	5.47
5H-3, 59	38.89	1.19	0.31	2.19	85.50	86.20	73.80	281.90	5.88	6.04
5H-4, 24	39.54	1.22	0.37	2.29	83.60	84.30	70.00	233.20	5.10	5.22
6H-1, 69	45.49	1.18	0.30	2.13	85.60	86.30	74.60	293.10	5.92	6.09
6H-1, 135	46.15	1.25	0.40	2.39	83.10	83.70	68.30	215.20	4.90	5.01
6H-2, 69	46.99	1.21	0.35	2.28	84.40	85.10	71.40	249.30	5.42	5.55
6H-3, 69	48.49	1.25	0.40	2.39	82.70	83.40	67.70	209.90	4.80	4.90
6H-4, 69	49.99	1.31	0.48	2.51	80.40	81.00	63.10	170.70	4.11	4.18
6H-5, 69	51.49	1.30	0.47	2.55	81.10	81.80	63.80	176.20	4.30	4.39
6H-6, 69	52.99	1.29	0.46	2.49	81.30	82.00	64.70	183.00	4.36	4.45
6H-7, 39	54.19	1.25	0.37	2.61	85.30	85.90	70.00	233.70	5.80	5.95
7H-1, 109	55.39	1.25	0.38	2.47	84.10	84.70	69.20	224.30	5.28	5.41
7H-2, 69	56.49	1.44	0.69	2.61	73.40	73.90	52.20	109.30	2.75	2.79
7H-3, 69	57.99	1.45	0.69	2.74	74.50	75.10	52.50	110.70	2.92	2.96
7H-4, 69	59.49	1.35	0.57	2.41	76.10	76.70	57.80	137.20	3.19	3.23
7H-5, 69	60.99	1.34	0.54	2.54	78.50	79.10	59.90	149.60	3.64	3.70
7H-5, 133	61.63	1.32	0.48	2.63	81.20	81.80	63.20	171.60	4.33	4.41
7H-6, 69	62.49	1.33	0.53	2.42	77.70	78.30	60.00	150.20	3.48	3.54
7H-7, 24	63.54	1.42	0.65	2.61	74.80	75.40	54.10	118.00	2.97	3.01
8H-1, 69	64.49	1.35	0.54	2.59	78.90	79.50	60.10	150.70	3.75	3.81
8H-2, 69	65.99	1.35	0.51	2.81	81.40	82.00	62.00	163.00	4.38	4.47
8H-3, 69	67.49	1.37	0.52	3.16	83.00	83.60	61.90	162.60	4.90	5.01
8H-4, 69	68.99	1.35	0.48	3.22	84.70	85.20	64.30	179.90	5.52	5.66
8H-5, 69	70.49	1.34	0.47	3.14	84.70	85.30	65.00	185.40	5.53	5.67
8H-6, 69	71.99	1.32	0.44	3.08	85.20	85.80	66.30	196.30	5.75	5.90

Table 17. Vane shear strength data from Hole 885A.

Core, section, interval (cm)	Depth (mbsf)	Shear strength (kPa)
145-885A-		
1H-1, 110	1.10	11.30
1H-2, 110	2.60	12.34
1H-3, 110	4.10	14.22
2H-1, 110	5.70	17.15
2H-2, 115	7.25	19.03
2H-3, 110	8.70	16.31
2H-4, 110	10.20	19.24
2H-5, 110	11.70	18.62
2H-6, 110	13.20	17.36
3H-1, 105	15.15	35.25
3H-2, 115	16.75	14.43
3H-3, 110	18.20	15.69
3H-4, 110	19.70	15.48
3H-5, 110	21.20	46.53
3H-6, 110	22.70	50.28
4H-1, 110	24.70	57.79
4H-2, 110	26.20	101.31
4H-3, 110	27.70	75.80
4H-4, 110	29.20	65.29
4H-5, 110	30.70	76.55
4H-6, 110	32.20	61.54
5H-1, 110	34.20	57.04
5H-2, 110	35.70	53.28
5H-3, 110	37.20	61.54
5H-4, 110	38.70	62.29
5H-5, 110	40.20	66.79
5H-6, 110	41.70	83.30
6H-1, 110	43.70	62.29
6H-2, 110	45.20	67.54
6H-3, 110	46.70	73.55
6H-4, 110	48.20	57.04
6H-5, 110	49.70	54.78
6H-6, 110	51.20	49.53

Table 18. Vane shear strength data from Hole 886A.

Core, section, interval (cm)	Depth (mbsf)	Shear strength (kPa)
145-886-A-		
1H-1, 120	1.20	4.39
1H-2, 120	2.70	9.20
1H-3, 120	4.20	13.18
1H-4, 120	5.70	11.71
1H-5, 120	7.20	14.85
1H-6, 120	8.70	16.94

Table 19. Vane shear strength data from Hole 886B.

Core, section, interval (cm)	Depth (mbsf)	Shear strength (kPa)
145-886B-		
1H-1, 102	1.02	9.41
2H-1, 110	2.90	16.52
2H-2, 110	4.40	16.31
2H-3, 110	5.90	17.78
2H-4, 110	7.40	12.13
2H-5, 110	8.90	17.36
2H-6, 110	10.40	14.43
3H-1, 110	12.40	16.94
3H-2, 110	13.90	17.99
3H-3, 110	15.40	18.62
3H-4, 110	16.90	23.84
3H-5, 110	18.40	20.71
3H-6, 110	19.90	18.20
4H-1, 110	21.90	17.78
4H-2, 110	23.40	24.47
4H-3, 110	24.90	21.12
4H-4, 110	26.40	17.57
4H-5, 110	27.90	23.01
4H-6, 110	29.40	23.22
5H-1, 110	31.40	40.81
5H-2, 110	32.90	39.42
5H-3, 110	34.40	40.81
5H-4, 110	35.90	38.49
5H-5, 110	37.40	34.32
5H-6, 110	38.90	41.28
6H-1, 110	40.90	41.28
6H-2, 110	42.40	36.64
6H-3, 110	43.90	30.15
6H-4, 110	45.40	34.78
6H-5, 110	46.90	41.28
7H-1, 110	50.40	38.03
7H-2, 110	51.90	52.41
7H-3, 115	53.45	64.54
7H-4, 110	54.90	55.54
7H-5, 110	56.40	54.03
7H-6, 110	57.90	58.54

Table 20. Vane shear strength data from Hole 886C.

Core, section, interval (cm)	Depth (mbsf)	Shear strength (kPa)
145-886C-		
1H-1, 110	1.10	6.27
1H-2, 110	2.60	10.67
1H-3, 110	4.10	12.76
1H-4, 110	5.60	14.85
2H-1, 110	7.90	16.11
2H-2, 15	8.45	15.69
2H-3, 110	10.90	17.99
2H-4, 97	12.27	18.20
2H-5, 110	13.90	20.08
2H-6, 70	15.00	22.17
3H-1, 110	17.40	25.97
3H-2, 85	18.65	26.44
3H-3, 110	20.40	27.83
3H-4, 110	21.90	33.86
3H-5, 95	23.25	33.86
3H-5, 120	23.50	38.96
4H-1, 110	26.90	23.19
4H-2, 110	28.40	9.28
4H-3, 110	29.90	15.30
4H-4, 110	31.40	26.44
4H-5, 110	32.90	29.68
4H-6, 80	34.10	25.04
4H-6, 90	34.20	34.78
5H-1, 110	36.40	22.73
5H-2, 110	37.90	22.26
5H-3, 90	39.20	21.80
6H-1, 110	45.90	21.33
6H-2, 110	47.40	19.48
6H-3, 100	48.80	25.04
6H-4, 110	50.40	37.57
6H-5, 110	51.90	39.42
6H-6, 110	53.40	39.42
7H-2, 110	56.90	59.29
7H-3, 110	58.40	57.79
7H-4, 110	59.90	55.54
7H-5, 110	61.40	54.78
7H-6, 110	62.90	56.29
8H-1, 110	64.90	57.79
8H-2, 110	66.40	62.29
8H-3, 110	67.90	63.04
8H-4, 110	69.40	62.29
8H-5, 110	70.90	70.54

Table 21. Thermal conductivity data from Site 885/886.

Core, section, interval (cm)	Depth (mbsf)	Thermal conductivity (W/[m·°C])
145-885A-		
1H-2, 75	2.25	1.01
2H-2, 75	6.85	1.01
2H-4, 75	9.85	0.91
2H-6, 75	12.85	0.85
3H-2, 75	16.35	0.92
3H-4, 75	19.35	0.83
3H-6, 75	22.35	0.77
3H-2, 75	16.35	0.89
3H-4, 75	19.35	0.85
3H-6, 75	22.35	0.85
5H-2, 75	35.35	0.94
5H-4, 75	38.35	0.81
5H-6, 75	41.35	0.88
6H-2, 75	44.85	1.01
6H-4, 75	47.85	1.03
6H-6, 75	50.85	0.83
145-886B-		
1H-1, 75	0.75	1.08
2H-2, 60	3.90	1.04
2H-4, 60	6.90	0.96
2H-6, 60	9.90	1.00
3H-2, 75	13.55	0.97
3H-4, 75	16.55	0.96
3H-6, 76	19.56	0.90
4H-2, 75	23.05	0.88
4H-4, 75	26.05	0.83
4H-6, 75	29.05	0.84
6H-2, 75	42.05	0.96
6H-4, 75	45.05	0.88
6H-6, 75	48.05	0.80
6H-6, 75	48.05	0.78
7H-2, 75	51.55	1.05
7H-2, 75	51.55	1.06
7H-4, 75	54.55	0.97
7H-6, 75	57.55	0.98
145-886C-		
1H-2, 75	2.25	1.08
1H-4, 75	5.25	0.94
1H-5, 60	6.60	1.01
2H-2, 70	9.00	1.00
2H-4, 70	12.00	0.95
2H-6, 50	14.80	0.85
3H-2, 70	18.50	0.93
3H-4, 70	21.50	0.84
3H-6, 60	24.40	0.84
4H-2, 70	28.00	0.81
4H-4, 70	31.00	0.85
4H-6, 60	33.90	0.78
5H-2, 70	37.50	0.95
5H-3, 60	38.90	0.88
6H-2, 70	47.00	0.84
6H-4, 70	50.00	0.94
6H-6, 70	53.00	0.99
7H-2, 70	56.50	1.19
7H-4, 70	59.50	0.98
7H-6, 70	62.50	0.95
8H-2, 70	66.00	1.02
8H-4, 70	69.00	0.85
8H-6, 40	71.70	0.80

Table 22. Compressional wave velocity data (DSV) from Site 885/886.

Core, section, interval (cm)	Depth (mbsf)	P-wave velocity (m/s)
145-885A-		
1H-1, 45	0.45	1488.2
1H-2, 40	1.90	1492.9
1H-3, 40	3.40	1507.2
2H-1, 70	5.30	1494.5
2H-2, 35	6.40	1497.7
2H-3, 75	8.40	1491.4
2H-4, 40	9.50	1492.9
2H-5, 40	11.00	1497.7
2H-6, 40	13.00	1526.8
3H-1, 65	15.00	1531.7
3H-2, 40	16.00	1533.4
3H-3, 40	18.00	1523.5
3H-4, 40	19.00	1533.4
3H-5, 40	20.00	1533.4
3H-6, 40	22.00	1496.1
4H-1, 50	24.00	1538.4
4H-2, 40	25.00	1530.1
4H-3, 40	27.00	1536.7
4H-4, 40	29.00	1538.4
4H-5, 50	30.00	1517.0
4H-6, 40	31.00	1555.3
5H-1, 40	33.00	1528.4
5H-2, 40	35.00	1536.7
5H-3, 40	36.00	1530.1
5H-4, 40	38.00	1543.4
5H-4, 40	38.00	1538.4
5H-6, 40	41.00	1508.9
6H-1, 40	43.00	1510.5
6H-2, 40	45.00	1499.3
6H-3, 40	46.00	1528.4
6H-4, 40	47.00	1504.0
6H-5, 40	49.00	1502.4
6H-6, 40	50.00	1491.4
6H-7, 20	52.00	1460.5
145-886B-		
2H-1, 45	0.45	1489.8
2H-1, 60	2.40	1492.9
2H-2, 40	3.70	1496.1
2H-3, 40	5.20	1496.1
2H-4, 40	6.70	1500.8
2H-5, 25	8.05	1499.3
2H-6, 40	9.70	1497.7
3H-1, 40	11.70	1492.9
3H-2, 40	13.20	1496.1
3H-3, 40	14.70	1504.0
3H-4, 40	16.20	1499.3
3H-5, 40	17.70	1541.8
3H-6, 35	19.15	1520.2
4H-1, 40	21.20	1535.1
4H-2, 40	22.70	1535.1
4H-3, 40	24.20	1546.8
4H-4, 40	25.70	1525.1
4H-5, 40	27.20	1541.8
4H-6, 40	28.70	1557.0
5H-1, 40	30.70	1536.7
5H-2, 40	32.20	1535.1
5H-3, 40	33.70	1536.7
5H-4, 40	35.20	1546.8
5H-5, 40	36.70	1540.1
5H-6, 40	38.20	1546.8
6H-1, 40	40.20	1538.4
6H-2, 40	41.70	1543.4
6H-3, 40	43.20	1538.4
6H-4, 40	44.70	1546.8
6H-5, 40	46.20	1548.5
7H-1, 35	49.65	1520.2
7H-2, 40	51.20	1497.7
7H-3, 40	52.70	1502.4
7H-4, 40	54.20	1517.0
7H-5, 40	55.70	1500.8
7H-6, 40	57.20	1510.5
145-886C-		
2H-3, 53	10.33	1504.0
2H-4, 52	11.82	1505.6
2H-5, 52	13.32	1505.6
2H-6, 20	14.50	1538.4
3H-1, 65	16.95	1515.3
3H-2, 30	18.10	1531.7
3H-3, 53	19.83	1533.4
3H-4, 53	21.33	1541.8
3H-5, 53	22.83	1530.1

Table 22 (continued).

Core, section, interval (cm)	Depth (mbsf)	P-wave velocity (m/s)
3H-6, 33	24.13	1528.4
4H-1, 53	26.33	1538.4
4H-2, 53	27.83	1540.1
4H-3, 53	29.33	1545.1
4H-4, 53	30.83	1538.4
4H-5, 53	32.33	1538.4
4H-6, 23	33.53	1536.7
5H-1, 78	36.08	1525.1
5H-2, 52	37.32	1548.5
5H-3, 40	38.70	1540.1
6H-1, 53	45.33	1548.5
6H-2, 53	46.83	1535.1
6H-3, 43	48.23	1525.1
6H-4, 53	49.83	1510.5
6H-5, 53	51.33	1517.0
6H-6, 53	52.83	1508.9
7H-2, 40	56.20	1502.4
7H-3, 40	57.70	1520.2
7H-4, 40	59.20	1510.5
7H-5, 40	60.70	1507.2
7H-6, 40	62.20	1517.0
8H-1, 40	64.20	1499.3
8H-2, 40	65.70	1489.8
8H-3, 40	67.20	1478.9
8H-3, 40	67.20	1488.2
8H-4, 40	68.70	1482.0
8H-5, 50	70.30	1472.7
8H-6, 40	71.70	1477.3

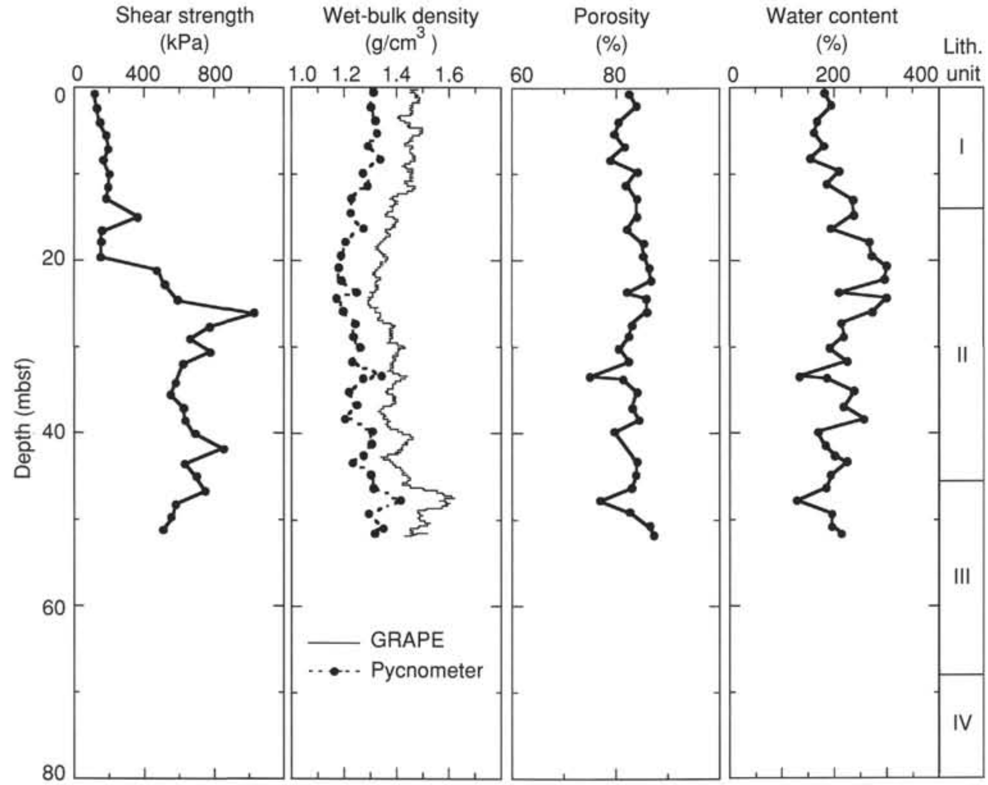

Figure 17. Index property and GRAPE data vs. depth for Hole 885A. Lithologic units are shown on the right.

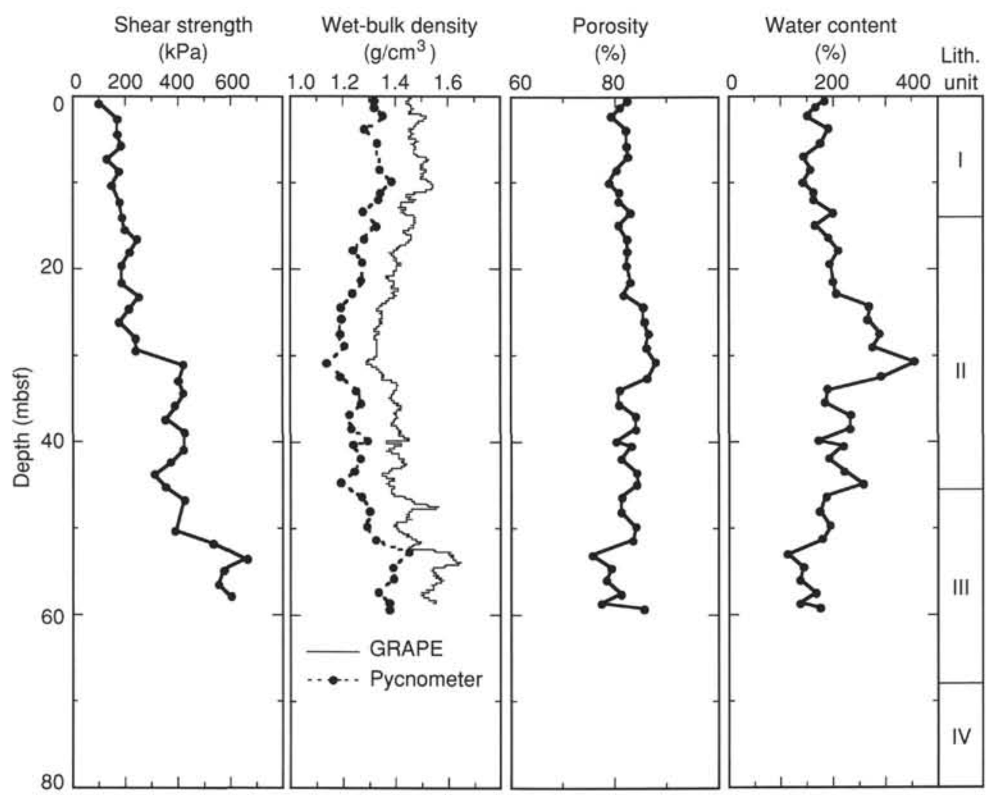

Figure 18. Index property and GRAPE data vs. depth for Hole 886B. Lithologic units are shown on the right.

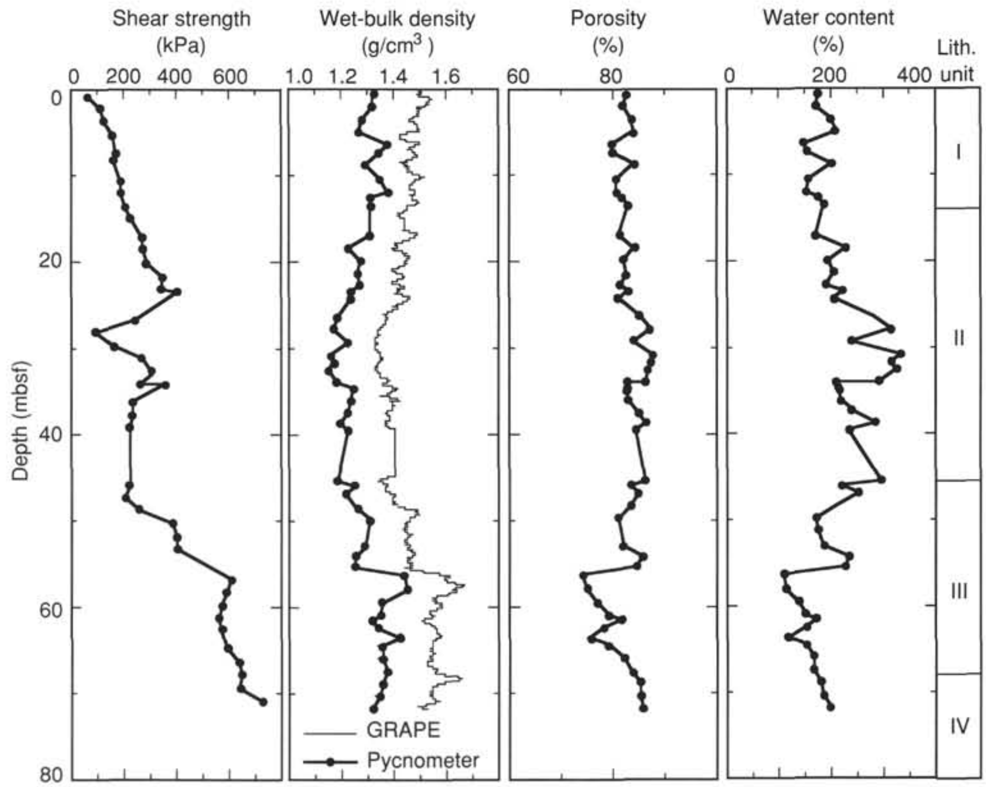

Figure 19. Index property and GRAPE data vs. depth for Hole 886C. Lithologic units are shown on the right.

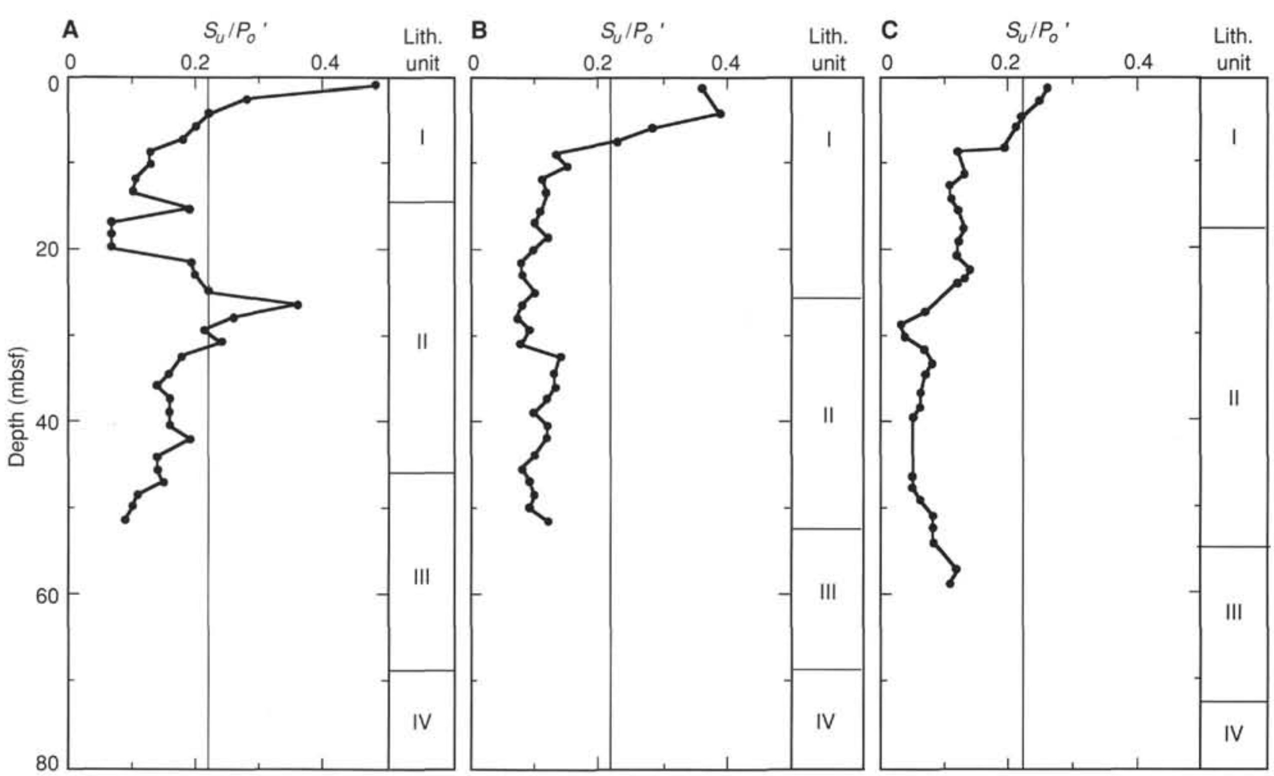

Figure 20. S_u/P_o' vs. depth. **A.** Hole 885A. **B.** Hole 886B. **C.** Hole 886C. Lithologic units are shown on the right.

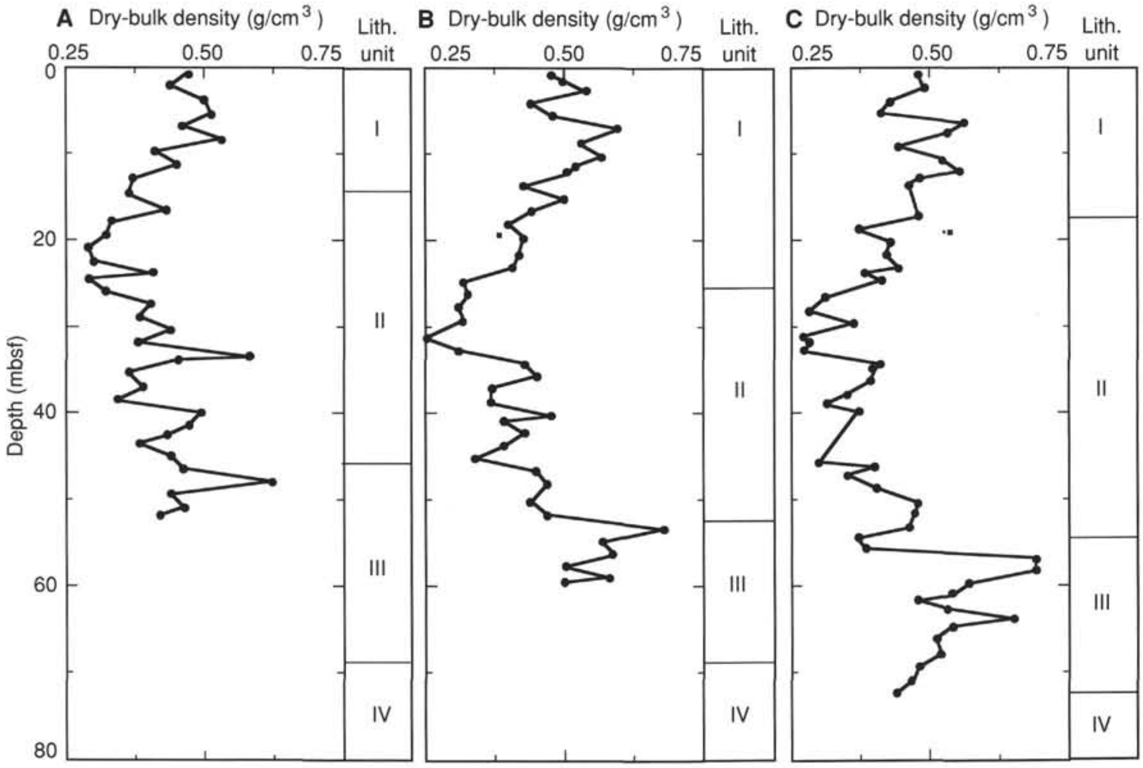

Figure 21. Dry-bulk density data vs. depth. **A.** Hole 885A. **B.** Hole 886B. **C.** Hole 886C. Lithologic units are shown on the right.

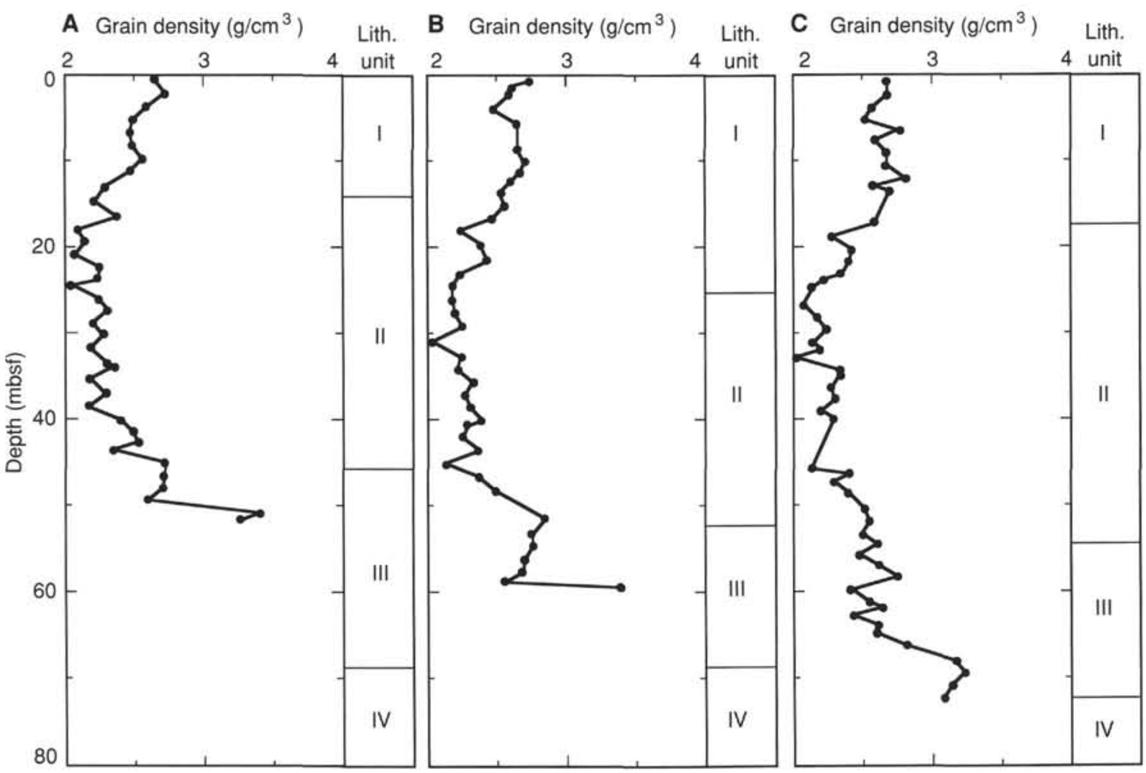

Figure 22. Grain density data vs. depth. **A.** Hole 885A. **B.** Hole 886B. **C.** Hole 886C. Lithologic units are shown on the right.

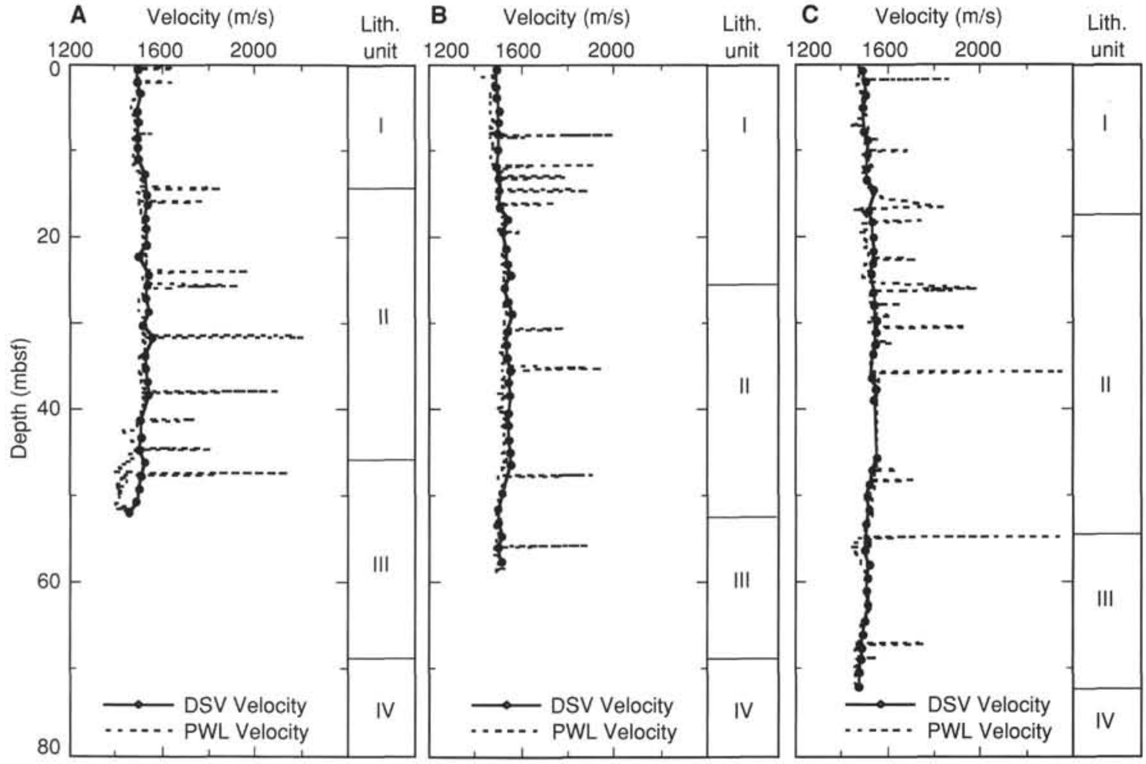

Figure 23. P-wave velocity data (DSV and PWL) vs. depth. **A.** Hole 885A. **B.** Hole 886B. **C.** Hole 886C. Lithologic units are shown on the right.

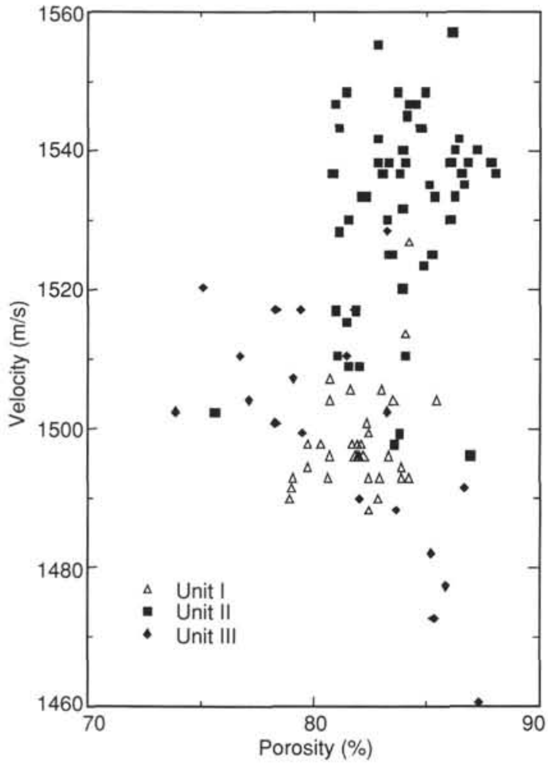

Figure 24. Compressional wave velocity data vs. dry porosity. **A.** Hole 885A. **B.** Hole 886B. **C.** Hole 886C.

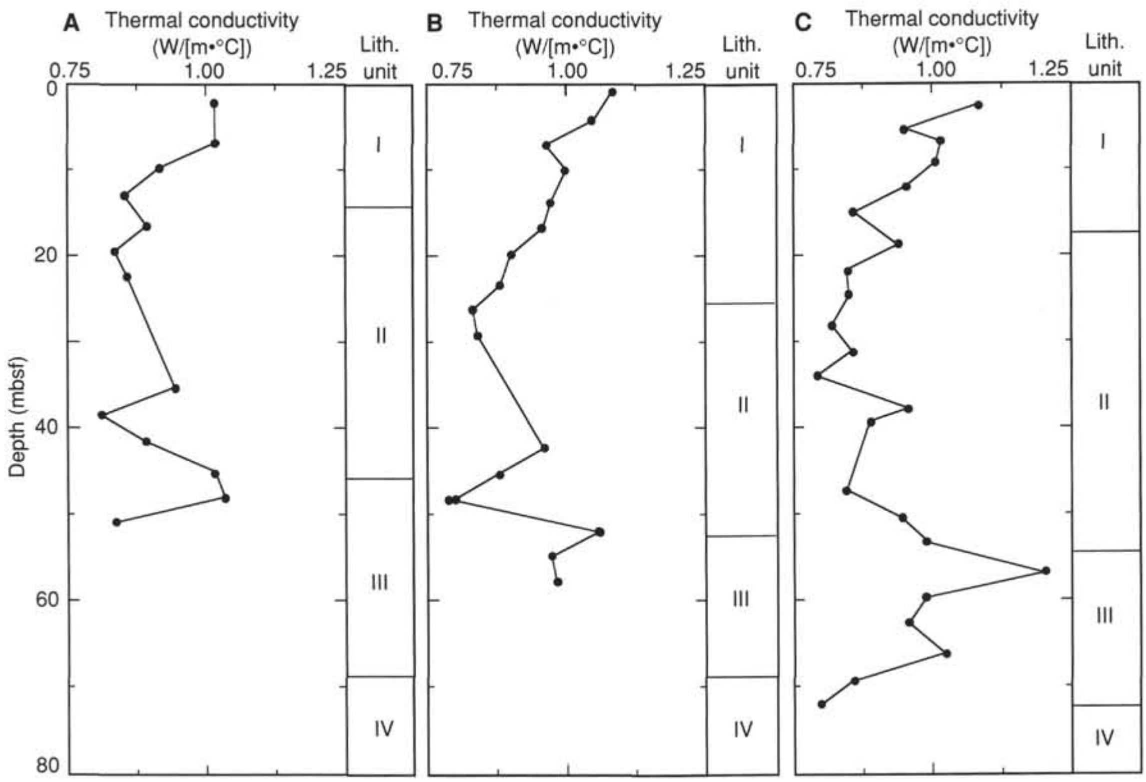

Figure 25. Thermal conductivity data vs. depth. **A.** Hole 885A. **B.** Hole 886B. **C.** Hole 886C. Lithologic units are shown on the right.

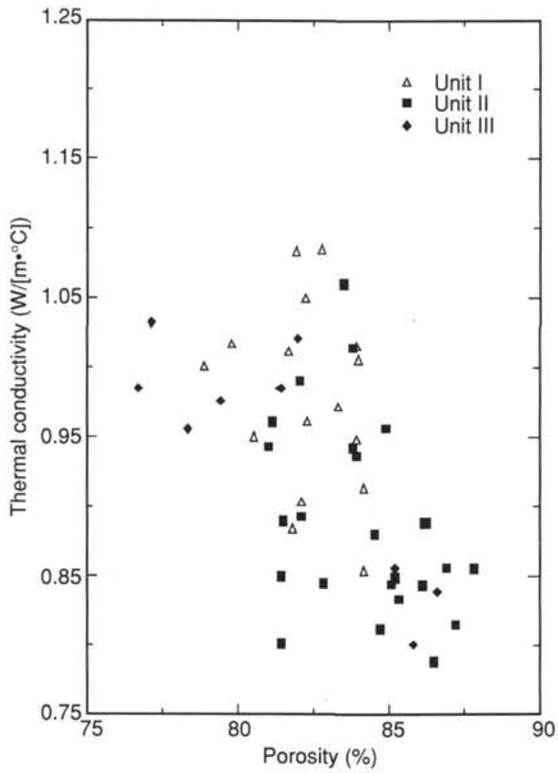

Figure 26. Thermal conductivity data vs. porosity for Holes 885A, 886B, and 886C.

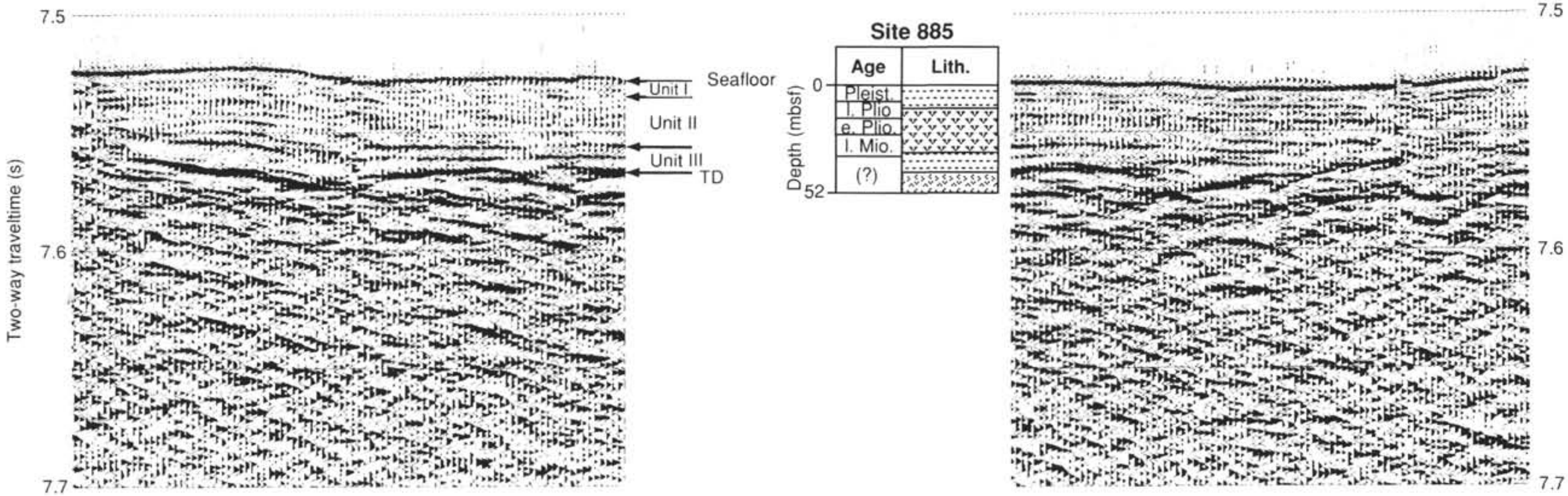

Figure 27. Processed seismic reflection profile from the *JOIDES Resolution* site-survey crossing Site 885. Line trends north-south, south is to the right. The depth ranges of lithologic Units I through III are indicated in the profile inset. Basalt was encountered at the bottom of the hole.

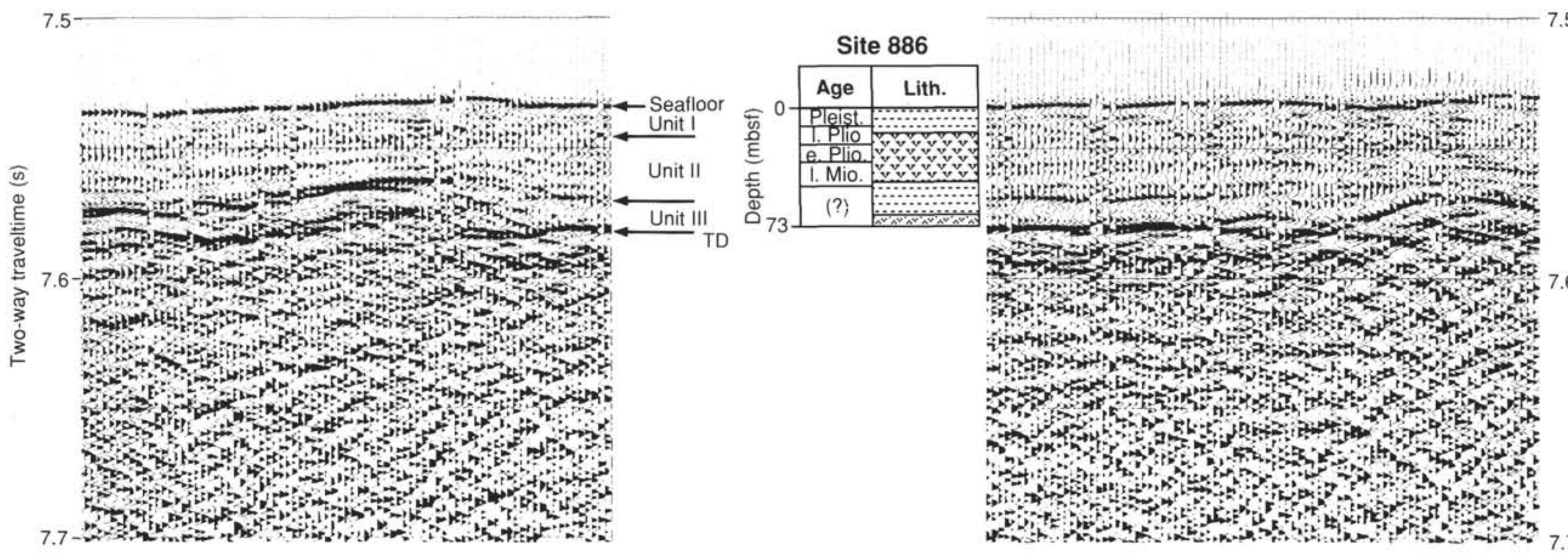

Figure 28. Processed seismic reflection profile from the *JOIDES Resolution* site-survey crossing Site 886. Line trends east-west, east is to the right. The depth ranges of lithologic Units I through III are indicated on the profile inset. Basalt was encountered at the bottom of the hole.